



Publication Year	2021
Acceptance in OA	2022-03-22T13:18:20Z
Title	The complex variability of blazars: time-scales and periodicity analysis in S4 0954+65
Authors	RAITERI, Claudia Maria, VILLATA, Massimo, Larionov, V M, Jorstad, S G, Marscher, A P, Weaver, Z R, Acosta-Pulido, J A, Agudo, I, Andreeva, T, Arkharov, A, Bachev, R, Benítez, E, Berton, M, Björklund, I, Borman, G A, Bozhilov, V, CARNERERO MARTIN, Maria Isabel, Carosati, D, Casadio, C, Chen, W P, Damljjanovic, G, D'AMMANDO, FILIPPO, Escudero, J, Fuentes, A, GIROLETTI, MARCELLO, Grishina, T S, Gupta, A C, Hagen-Thorn, V A, Hart, M, Hiriart, D, Hou, W-J, Ivanov, D, Kim, J-Y, Kimeridze, G N, Konstantopoulou, C, Kopatskaya, E N, Kurtanidze, O M, Kurtanidze, S O, Lähteenmäki, A, Larionova, E G, Larionova, L V, MARCHILI, Nicola, Markovic, G, Minev, M, Morozova, D A, Myserlis, I, Nakamura, M, Nikiforova, A A, Nikolashvili, M G, Otero-Santos, J, Ovcharov, E, Pursimo, T, Rahimov, I, RIGHINI, SIMONA, Sakamoto, T, Savchenko, S S, Semkov, E H, Shakhovskoy, D, Sigua, L A, Stojanovic, M, Strigachev, A, Thum, C, Tornikoski, M, Traianou, E, Troitskaya, Y V, Troitskiy, I S, Tsai, A, Valcheva, A, Vasilyev, A A, Vince, O, Zaharieva, E
Publisher's version (DOI)	10.1093/mnras/stab1268
Handle	http://hdl.handle.net/20.500.12386/31777
Journal	MONTHLY NOTICES OF THE ROYAL ASTRONOMICAL SOCIETY
Volume	504

The complex variability of blazars: time-scales and periodicity analysis in S4 0954+65

C. M. Raiteri¹★, M. Villata¹, V. M. Larionov^{2,3}, S. G. Jorstad^{2,4}, A. P. Marscher⁴, Z. R. Weaver⁴, J. A. Acosta-Pulido^{5,6}, I. Agudo⁷, T. Andreeva⁸, A. Arkharov³, R. Bachev⁹, E. Benítez¹⁰, M. Berton^{11,12}, I. Björklund^{12,13}, G. A. Borman¹⁴, V. Bozhilov¹⁵, M. I. Carnerero¹, D. Carosati^{16,17}, C. Casadio^{18,19,20}, W. P. Chen²¹, G. Damjanovic²², F. D’Ammando²³, J. Escudero⁷, A. Fuentes⁷, M. Giroletti²³, T. S. Grishina², A. C. Gupta²⁴, V. A. Hagen-Thorn², M. Hart⁴, D. Hiriart²⁵, W.-J. Hou²¹, D. Ivanov⁸, J.-Y. Kim²⁶, G. N. Kimeridze²⁷, C. Konstantopoulou^{28,29}, E. N. Kopatskaya², O. M. Kurtanidze^{27,30,31}, S. O. Kurtanidze^{27,30,32}, A. Lähteenmäki^{12,13}, E. G. Larionova², L. V. Larionova², N. Marchili²³, G. Markovic³³, M. Mineev¹⁵, D. A. Morozova², I. Myserlis^{12,13}, M. Nakamura³⁵, A. A. Nikiforova^{2,3}, M. G. Nikolashvili^{27,30}, J. Otero-Santos^{5,6}, E. Ovcharov¹⁵, T. Pursimo²⁸, I. Rahimov⁸, S. Righini²³, T. Sakamoto³⁵, S. S. Savchenko^{2,3,36}, E. H. Semkov⁹, D. Shakhovskoy¹⁴, L. A. Sigua²⁷, M. Stojanovic²², A. Strigachev⁹, C. Thum³⁴, M. Tornikoski¹², E. Traianou²⁰, Y. V. Troitskaya², I. S. Troitskiy², A. Tsai²¹, A. Valcheva¹⁵, A. A. Vasilyev², O. Vince²² and E. Zaharieva¹⁵

Affiliations are listed at the end of the paper

Accepted 2021 April 30. Received 2021 April 29; in original form 2021 March 22

ABSTRACT

Among active galactic nuclei, blazars show extreme variability properties. We here investigate the case of the BL Lac object S4 0954+65 with data acquired in 2019–2020 by the *Transiting Exoplanet Survey Satellite* (*TESS*) and by the Whole Earth Blazar Telescope (WEBT) Collaboration. The 2-min cadence optical light curves provided by *TESS* during three observing sectors of nearly 1 month each allow us to study the fast variability in great detail. We identify several characteristic short-term time-scales, ranging from a few hours to a few days. However, these are not persistent, as they differ in the various *TESS* sectors. The long-term photometric and polarimetric optical and radio monitoring undertaken by the WEBT brings significant additional information, revealing that (i) in the optical, long-term flux changes are almost achromatic, while the short-term ones are strongly chromatic; (ii) the radio flux variations at 37 GHz follow those in the optical with a delay of about 3 weeks; (iii) the range of variation of the polarization degree and angle is much larger in the optical than in the radio band, but the mean polarization angles are similar; (iv) the optical long-term variability is characterized by a quasi-periodicity of about 1 month. We explain the source behaviour in terms of a rotating inhomogeneous helical jet, whose pitch angle can change in time.

Key words: galaxies: active – BL Lacertae objects: general – BL Lacertae objects: individual: S4 0954+65 – galaxies: jets.

1 INTRODUCTION

Blazars are active galactic nuclei that show extreme variability properties. They include flat-spectrum radio quasars, generally showing broad emission lines in their spectra, and (almost) featureless BL Lac objects. Blazar emission mostly comes from a relativistic plasma jet that is oriented closely to the line of sight. As a consequence, the flux is Doppler beamed and boosted, and time-scales are shortened. Blazar variability is unpredictable. Some objects show almost continuous activity, while others undergo extreme outburst events after periods of almost constant emission. Variability time-

scales range from years down to hours, likely implying that different mechanisms are at work, both of intrinsic (i.e. energetic) and extrinsic (i.e. geometric) nature.

The *Transiting Exoplanet Survey Satellite* (*TESS*; Ricker et al. 2015) that was launched in 2018, though dedicated to the discovery of exoplanets, gives us the possibility to study the short-term blazar variability with extremely dense sampling. Therefore, we proposed a number of bright blazars for *TESS* observations in cycles 2, 3, and 4. Some of these *TESS* blazar observations were supported by ground-based monitoring by the Whole Earth Blazar Telescope¹ (WEBT) Collaboration (e.g. Villata et al. 2002, 2004, 2006, 2008; Raiteri

* E-mail: claudia.raiteri@inaf.it

¹<http://www.oato.inaf.it/blazars/webt/>

et al. 2013, 2017b; Carnerero et al. 2015, 2017; Larionov et al. 2016, 2020), which in particular added colour information.

The 2-min cadence *TESS* observations of BL Lacertae were analysed by Weaver et al. (2020), together with data from the WEBT, and the *Neil Gehrels Swift*, the *Nuclear Spectroscopic Telescope Array (NuStar)*, and the *Fermi* satellites. The authors found that the shortest variability time-scale in the *TESS* light curve is about 0.5 h, while the most common time-scale is around 13 h. This is similar to the minimum time-scale identified in the X-rays, 14.5 h. They found a statistically significant correlation between the *TESS* and X-ray light curves, with X-ray variations lagging the optical ones up to ~ 0.4 d, and explained the source behaviour as due to a shock propagating in turbulent plasma.

In Raiteri et al. (2021) we analysed the short-term optical variability of the BL Lac object S5 0716+714 with both *TESS* and WEBT data. We found that the flux variations of this source have a dual nature. Variability on time-scales shorter than about 5 h shows a clear bluer-when-brighter behaviour and is likely due to energetic processes in jet regions of milliparsec size. Flux changes on time-scales longer than half a day are instead almost achromatic. We proposed a geometrical explanation for them. Since there are various variability time-scales, we suggested that the jet is made up of filaments twisting around the jet axis. Each filament has its own changing orientation with respect to the line of sight and thus its emission is affected by a variable Doppler factor.

We here apply the same methods used in that paper to the *TESS* and WEBT observations of another BL Lac object, S4 0954+65. The redshift of this source is still debated. A tentative estimate $z = 0.368$ was given by Lawrence et al. (1986) based on [O III] $\lambda\lambda 4959, 5007$ and galactic absorption lines. The value was essentially confirmed by Stickel, Fried & Kuehr (1993), who determined $z = 0.367$ from the identification of Ca II $\lambda\lambda 3933, 3968$ and extremely weak [O II] $\lambda 3727$. These redshift values have been questioned by Landoni et al. (2015), who claimed a lower limit of 0.45. However, recently Becerra González et al. (2021) gave a more precise estimate, $z = 0.3694 \pm 0.0011$, using the Mg II $\lambda 2800$ emission line visible during a faint state of the source.²

S4 0954+65 is well known for its fast flux changes. Intranight/intraday variability in the optical/radio band has been detected many times, especially when the source was in flaring state (Wagner et al. 1990, 1993; Heidt & Wagner 1996; Raiteri et al. 1999; Marchili et al. 2012; Morozova et al. 2014; Bachev 2015). In some of these studies, geometrical effects were invoked to explain at least part of the variability. During the 2008 radio outburst, the intraday variability properties were seen to change, with the appearance of multiple time-scales (Marchili et al. 2012). The source was first detected at very high energies (≥ 100 GeV) during an exceptionally bright state in 2015 February (MAGIC Collaboration 2018). Both the 2011 and 2015 outbursts were accompanied by wide rotations of the optical polarization angle and they were associated with the emission of new jet components observed in high-resolution radio images (Morozova et al. 2014; MAGIC Collaboration 2018). The swing of the polarization angle observed in 2011, from 0° to 330° and then back to 0° , was interpreted by Lyutikov & Kravchenko (2017) in terms of an oscillating circular motion.

Differently from the work done on S5 0716+714 by Raiteri et al. (2021), who analysed about 1 month of *TESS* and WEBT data, in this paper we explore *TESS* data coming from three observing sectors, lasting about 1 month each, and WEBT monitoring data extending

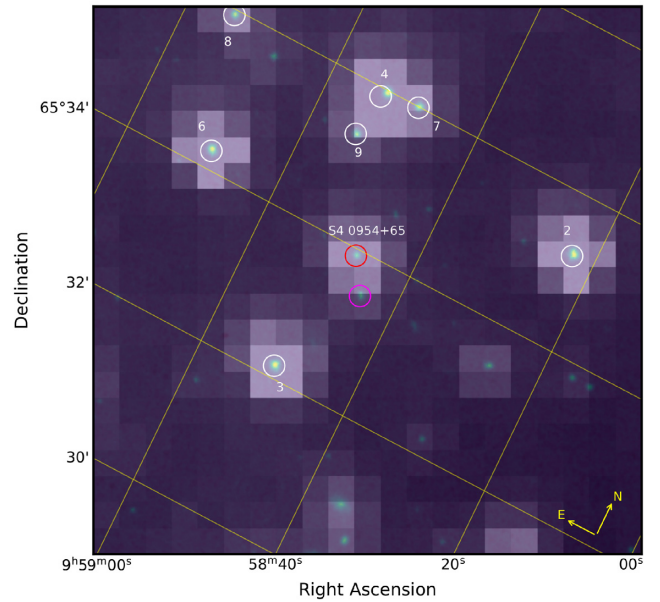


Figure 1. A 21×21 pixel cut-out of a *TESS* FFI centred on S4 0954+65 (red circle) from 2019 August 9 16:15:36 UT (large pixels). A Digitized Sky Survey 2 (red filter) image of the same field is shown in the background. Close comparison stars are circled in white and labelled according to Raiteri et al. (1999), while the nearby faint source is circled in magenta. Differences in the *TESS* locations (circles) and DSS PSFs can be reconciled by the proper motion of the sources.

to the whole 2019–2020 optical observing season. Moreover, WEBT data include now also radio photometric and radio and optical polarimetric observations. In this way we can investigate both short and long variability time-scales, from a few hours to several weeks, and put them in context, considering the source spectral and polarization variability.

The paper is structured as follows. In Section 2, we describe the *TESS* observations of S4 0954+65 during cycle 2. The data provided by the WEBT are presented in Section 3 (optical and near-infrared), and Section 5 (radio). The behaviour of colour indices is discussed in Section 4 and those of the polarization degree and angle in Section 6. A detailed analysis of the short-term variability in the *TESS* light curves is performed in Section 7, using the autocorrelation function (and structure function) and periodogram. The long-term variability in 1 yr of WEBT and *TESS* observations is studied in Section 8. A rotating helical jet model is applied to the optical observations in Section 9. The results are summarized in Section 10, where the conclusions are finally drawn.

2 OBSERVATIONS BY TESS

Blazar S4 0954+65 was observed by the *TESS* satellite during its cycle 2, targeting the northern ecliptic sky. The source was monitored in Sector 14 (2019 July 18.84–August 14.70), and then in Sector 20 (2019 December 25.01–2020 January 20.33) and 21 (2020 January 21.93–2020 February 18.28).

Given the large pixel size of the *TESS* detector, crowded fields may complicate the analysis of blazar light curves. Fig. 1 shows a cut-out of a *TESS* Full Frame Image (FFI) taken during Sector 14 and centred on S4 0954+65. All main comparison stars from Raiteri et al. (1999) are sufficiently far from the source and do not have PSFs that overlap. A single faint star to the south-west does overlap with the blazar in the algorithm-determined 2-min cadence aperture of each

²They also identified the [O III], and possibly the [O II] emission lines.

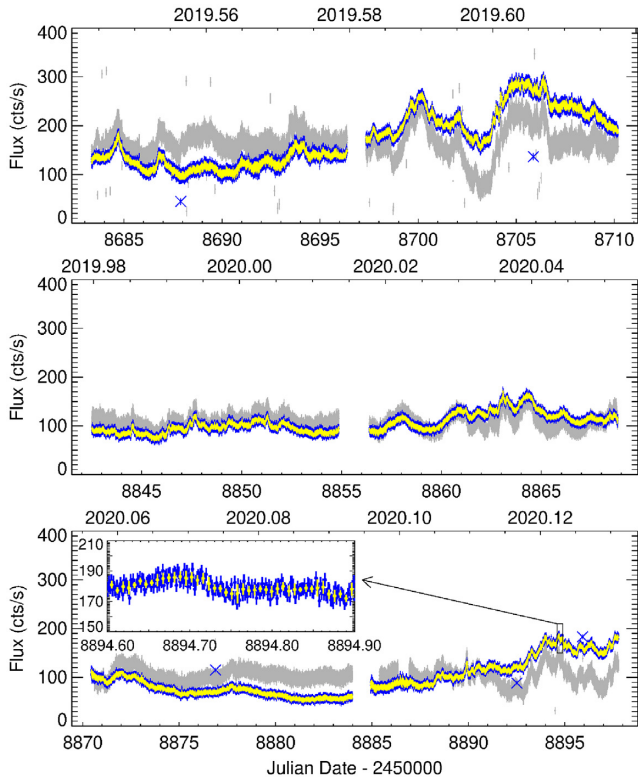


Figure 2. *TESS* light curves of S4 0954+65 during Sector 14 (top), 20 (middle), and 21 (bottom). Fluxes are given as electrons per second. The blue dots and bars represent the 2-min cadence simple-aperture photometry fluxes (SAP_FLUX) and errors; the blue crosses indicate the outliers that have been removed before binning; the yellow points and bars show the 10-min binned fluxes and their standard deviations. The grey dots and bars represent conditioned fluxes (PDCSAP_FLUX) and errors. In the inset panel a zoom into the Sector 21 light curve shows in more details the effect of the 10-min binning.

observing sector. However, taking the PSF of the source into account, this aperture captures approximately two-thirds of the total estimated flux from S4 0954+65. Given that the blazar is relatively isolated from nearby stars and that the majority of light in the automatically determined aperture comes from the source, we conclude that there are no systematic issues due to flux contamination to correct for.

The 2-min cadence light curves are shown in Fig. 2. They were downloaded from the Mikulski Archive for Space Telescopes.³ There is a remarkable difference in trend between the simple-aperture photometry fluxes (SAP_FLUX) and the pre-search data conditioned simple aperture photometry fluxes (PDCSAP_FLUX). With respect to the former, the latter were further processed to remove possible instrumental effects that are known to affect light curves of stars that are exoplanets host candidates. This translates into removing long-term trends. However, this process may erase true source variability in objects like blazars. Moreover, the PDCSAP_FLUX data points show much more scatter and outliers, especially during Sector 14. We will show in Section 3 that ground-based optical data confirm the reliability of the SAP_FLUX light curves.

Because of the source relative faintness, the *TESS* light curves are somewhat noisy. Therefore, we first removed the most evident outliers by discarding those data points that are out of 4 standard

deviations in the 0.1 d binned light curve. Then we binned the SAP fluxes in time intervals of 10 min and assumed the standard deviation in each bin as the data uncertainty (see Fig. 2). In the rest of the paper we will use these 10-min binned SAP fluxes, including 11 097 data points.

3 OPTICAL AND NEAR-INFRARED OBSERVATIONS BY THE WEBT

To increase the scientific return of the *TESS* observations, the WEBT Collaboration organized a multiwavelength monitoring campaign. In this section, we present the optical and near-infrared data acquired by the WEBT over a whole year including the *TESS* pointings, from 2019 July 18 to 2020 July 18 (JD = 2458683–2459049). Table 1 lists the participating observatories.

In the optical band, 1764 data in the *BVRIZ* filters were taken with 20 telescopes around the world, with diameters from 35 to 260 cm. Nearly 64 percent of the optical data are in the Cousins’ *R* filter, which will be considered our reference band. Data were reduced according to standard prescriptions. The source magnitude was calibrated with respect to the photometric sequence by Raiteri et al. (1999) in *BVRI* and using PanSTARRS⁴ PS1 magnitudes for the few data acquired with the Nordic Optical Telescope (NOT) in the Sloan Digital Sky Survey⁵ (SDSS) *z* band. A few near-infrared observations were done with the 2 m Liverpool telescope in *H* band. Calibration of these data was obtained using Two Micron All Sky Survey⁶ (2MASS) sources in the field.

In the *BVRI* bands, the different data sets were combined and the resulting multiband light curves were visually inspected and processed to obtain homogeneous and reliable curves for further analysis. We eliminated clear outliers and reduced data noise by binning data close in time from the same telescope, when appropriate. In only three cases we had to apply shifts to align the data sets with the trend traced by all the others. The final optical light curves are shown in Fig. 3. They reveal continuous activity, with variability amplitudes (max – min) of 2.48, 2.00, 2.82, 2.61 mag in *BVRI* bands, respectively. Although much less sampled, the magnitude range spanned in the *z* and *H* bands are 1.12 and 1.18, respectively.

We note that the larger values in the *R* and *I* bands are due to a remarkable variability episode occurred on JD = 2458740–42, when the source brightened by 1.0 mag in 24 h in the *R* band, and then dimmed by 0.8 mag in 23 h. We carefully checked the reliability of this episode, which is also visible in the *I* band, and found no reasons to distrust it. Though rather extreme, this event is not unique, as e.g. a brightening of about 0.9 mag in 24 h was observed by Raiteri et al. (2009) in 2007, during a WEBT campaign targeting BL Lacertae. Without this episode, the variability amplitudes of S4 0954+65 in *R* and *I* bands are 2.46 and 2.24 mag, respectively.

Fig. 3 also shows the periods of *TESS* observations and the *TESS* fluxes converted into *R*-band magnitudes. These *TESS* magnitudes adapted to the reference *R* band will be used in the following to perform time series analysis on the composite light curve, including both *TESS* and WEBT data. The transformation of the *TESS* fluxes into magnitudes was done by taking into account that the *TESS* detector bandpass,⁷ which is very wide, spanning from 600 to 1000 nm, is centred on the Cousins’ *I* band. As we saw above, the variability

⁴<https://panstarrs.stsci.edu/>

⁵<https://www.sdss.org/>

⁶<https://irsa.ipac.caltech.edu/Missions/2mass.html>

⁷<https://heasarc.gsfc.nasa.gov/docs/tess/the-tess-space-telescope.html>

³<https://mast.stsci.edu/portal/Mashup/Clients/Mast/Portal.html>

Table 1. Observatories contributing data to the WEBT campaign on S4 0954+65.

Observatory	Country	Tel. size (cm)	Band	Symbol	Colour
<i>Optical</i>					
Abastumani	Georgia	70	<i>R</i>	◇	dark green
Aoyama-Gakuin	Japan	35	<i>BVRI</i>	△	brown
ARIES	India	130	<i>BRI</i>	◇	orange
Belogradchik	Bulgaria	60	<i>BVRI</i>	◇	blue
Crimean ^a	Russia	70	<i>BVRI</i>	×	blue
Crimean ^b	Russia	70	<i>BVRI</i>	+	magenta
Crimean ^c	Russia	260		◇	green
Haleakala ^d	US	40	<i>R</i>	★	red
Lulin	Taiwan	40	<i>R</i>	◦	cyan
McDonald ^d	US	40	<i>R</i>	★	green
Perkins	US	180	<i>BVRI</i>	◇	magenta
Roque de los Muchachos ^e	Spain	260	<i>BVRIZ</i>	◦	black
Rozhen	Bulgaria	50/70	<i>BVRI</i>	◇	black
Rozhen	Bulgaria	200	<i>BVRI</i>	□	black
San Pedro Martir	Mexico	84	<i>R</i>	×	black
St. Petersburg	Russia	40	<i>BVRI</i>	×	red
Teide ^d	Spain	40	<i>R</i>	★	black
Teide	Spain	80	<i>BVRI</i>	◦	red
Tijarafe	Spain	40	<i>R</i>	+	dark green
Vidojevića ^f	Serbia	60	<i>BVRI</i>	△	green
Vidojevića ^f	Serbia	140	<i>BVRI</i>	◦	green
<i>Near-infrared</i>					
Roque de los Muchachos ^g	Spain	200	<i>H</i>	◇	red
Observatory	Country	Tel. size (m)	Band (GHz)	Symbol	Colour
<i>Radio</i>					
Cagliari ^h	Italy	64	6.0	+	magenta
Cagliari ^h	Italy	64	24	△	black
Medicina	Italy	32	8.5	×	black
Metsähovi	Finland	14	37	◇	blue
Pico Veleta	Spain	30	230	□	blue
Pico Veleta	Spain	30	86	◦	black
Svetloe	Russia	32	8.5	×	blue
Svetloe	Russia	32	4.8	◦	orange

^aST-7 detector.^bAP7p detector.^cOnly polarization.^dWithin Las Cumbres Observatory global telescope network.^eNordic Optical Telescope (NOT).^fAstronomical Station Vidojevića.^gLiverpool Telescope.^hSardinia Radio Telescope (SRT).

amplitude in S4 0954+65 is likely to increase from the *I* to the *R* band, so a simple flux-to-magnitude formula $\text{mag}_{TESS} = -2.5 \log(\text{SAP_FLUX}) + \text{mag}_0$ cannot reproduce the whole magnitude range observed in the *R* band (see Fig. 4, where mag_0 is set to 20.75 to obtain a good match). Therefore, we first ‘stretched’ the *TESS* fluxes and then converted them into magnitudes, according to: $\text{mag}_{TESS} = -2.5 \log(\text{SAP_FLUX})^\zeta + \text{mag}_0$ (see also Raiteri et al. 2021). To find the best-fitting values for ζ and mag_0 , we built a grid of 100×100 *TESS* light curves, changing ζ and mag_0 in steps of 0.01, and found the case which minimized the root mean square of the mag differences between the closest WEBT and *TESS* data points. The *TESS* observations in Sector 14 occurred near the source solar conjunction and only a few WEBT data are available; those

in Sectors 20 and 21 were supported by the WEBT core campaign, during which an exceptional sampling was reached in the *R* band. For the best-sampled period of Sector 20 + 21, we got $\zeta = 1.27$ and $\text{mag}_0 = 22.08$. As for Sector 14, we fixed $\zeta = 1.27$ and derived $\text{mag}_0 = 22.28$. The reason why there is an offset of 0.2 mag between Sector 14 and Sector 20 + 21 is due to *TESS* calibration problems, particularly to the fact that the source was imaged in Camera 4 during Sector 14, but in Camera 2 in Sector 20 + 21. The result of our procedure is shown in Fig. 4 and highlights the excellent match between *TESS* and WEBT data obtained. Incidentally, the WEBT data confirm that in the case of S4 0954+65 the SAP fluxes are the right quantities to consider (see also Raiteri et al. 2021) instead of the PDCSAP fluxes.

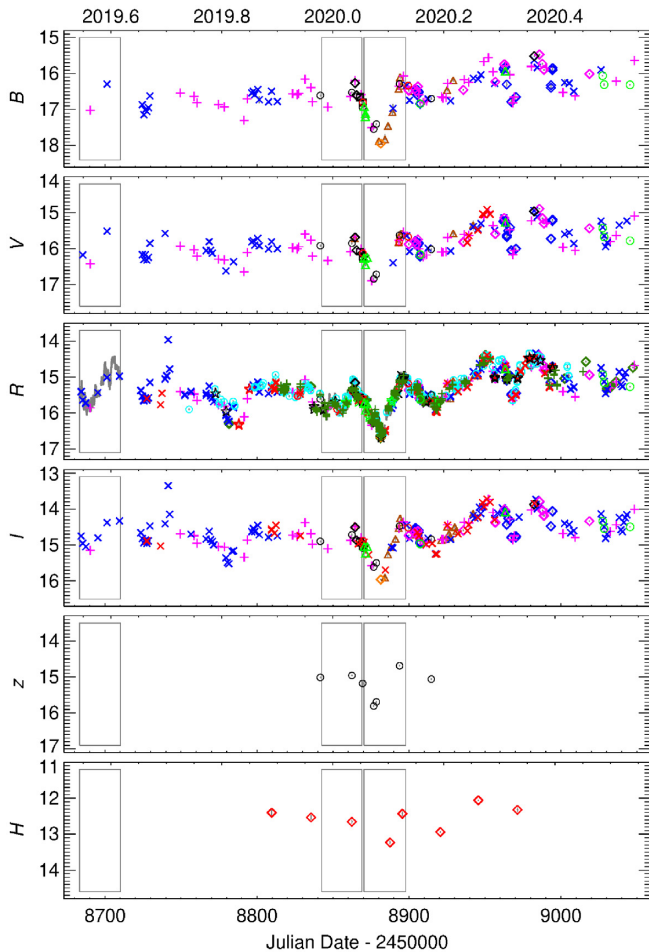


Figure 3. Multiband optical light curves of S4 0954+65 by the WEBT Collaboration. Different symbols and colours distinguish different observatories and telescopes, as listed in Table 1. The grey boxes mark the periods of TESS observations and the grey dots in the R-band panel represent the TESS SAP fluxes converted into R-band magnitudes as explained in the text.

4 OPTICAL COLOURS

Blazars are known also for their spectral variability, which often shows trends with brightness. In particular, BL Lac objects usually follow a bluer-when-brighter behaviour, especially during fast flares (e.g. Villata et al. 2004; Wu et al. 2005; Larionov, Villata & Raiteri 2010; Cheng, Zhang & Xu 2013; Agarwal et al. 2015; Hagen-Thorn et al. 2015; Raiteri et al. 2015, 2021). In Raiteri et al. (2021), we found that the short-term variability of another BL Lac object, S5 0716+714, presents a double nature. Flux changes on time-scales less than a few hours are strongly chromatic and are likely due to energetic processes occurring in small (milliparsec scale) jet zones, while those on time-scales longer than about half a day are quasi-achromatic and are most likely the consequence of changes in the orientation of the jet emitting regions with respect to the line of sight.

To analyse the spectral optical variability of S4 0954+65 in the period considered in this paper, we combine the WEBT BVRI data to build colour indices. The prescription is to use pairs of good data (with uncertainties less than 0.03 mag) acquired from the same telescope within 20 min. We obtained 82 $B - R$, 159 $R - I$, and 123 $V - I$ colour indices, with average values of 1.14 ± 0.08 , 0.68 ± 0.04 , and 1.20 ± 0.06 , respectively. From the $V - I$ index, by transforming

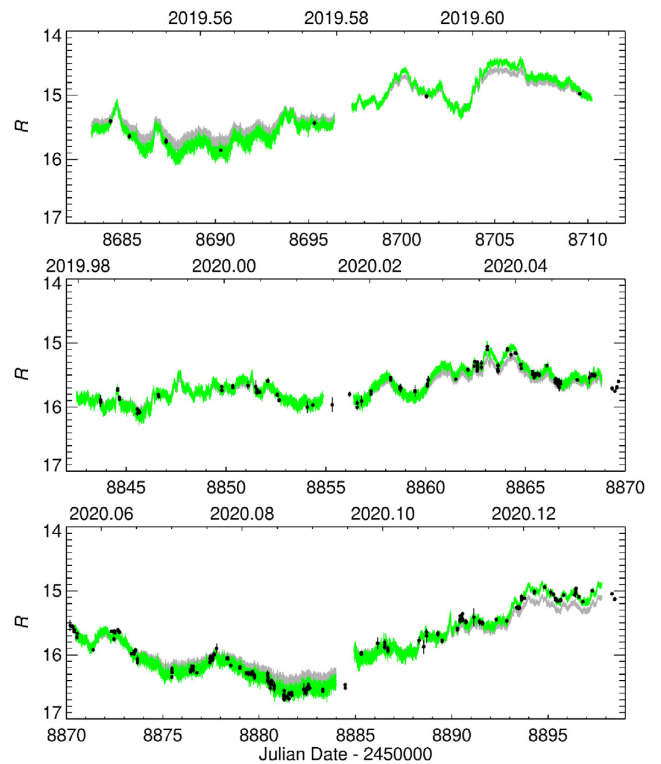


Figure 4. The R-band light curve in TESS Sector 14 (top), Sector 20 (middle), and Sector 21 (bottom). The black dots represent WEBT data. The grey dots show TESS SAP fluxes converted into magnitudes according to the simple formula $\text{mag}_{\text{TESS}} = -2.5 \log(\text{SAP_FLUX}) + \text{mag}_0$, with $\text{mag}_0 = 20.75$. Because of the TESS spectral response, this is not able to reproduce the R-band variability amplitude. The green dots show the TESS fluxes converted into R-band magnitudes according to $\text{mag}_{\text{TESS}} = -2.5 \log(\text{SAP_FLUX})^\zeta + \text{mag}_0$, with best-fitting values $\zeta = 1.27$ and $\text{mag}_0 = 22.08$ in Sectors 20 + 21, and $\text{mag}_0 = 22.28$ in Sector 14.

magnitudes into dereddened flux densities⁸ and adopting a power-law $F_\nu \propto \nu^{-\alpha}$ to describe the spectral shape, we obtain an average index $\alpha = 1.82 \pm 0.15$, which implies a steep optical spectrum.

Fig. 5 compares the behaviour of brightness in the I band and $V - I$ colour as a function of time, and shows the colour (and spectral index) versus brightness. A linear fit indicates a slope of 0.07 and the correlation coefficient is only 0.52. As a consequence, we can say that the long-term spectral variability of S4 0954+65 is only mildly chromatic, with a hint of a bluer-when-brighter behaviour. These quasi-achromatic variations can be explained by changes of the Doppler factor, if the optical spectral slope is approximately constant. Alternatively, they can be ascribed to a change in the plasma density, or to a variation in the magnetic field strength, again if the optical spectral index were roughly constant, and radiative losses did not increase. In contrast, the short-term brightness changes display a pronounced chromatism, as most notably visible around $\text{JD} - 2450000 = 8905$ and 8965 in Fig. 5. The bad linear fit itself is the consequence of these fast chromatic variations.

⁸Adopting the absolute fluxes by Bessell, Castelli & Plez (1998) and the values for the Galactic extinction from the NASA/IPAC Extragalactic Database, <https://ned.ipac.caltech.edu/>

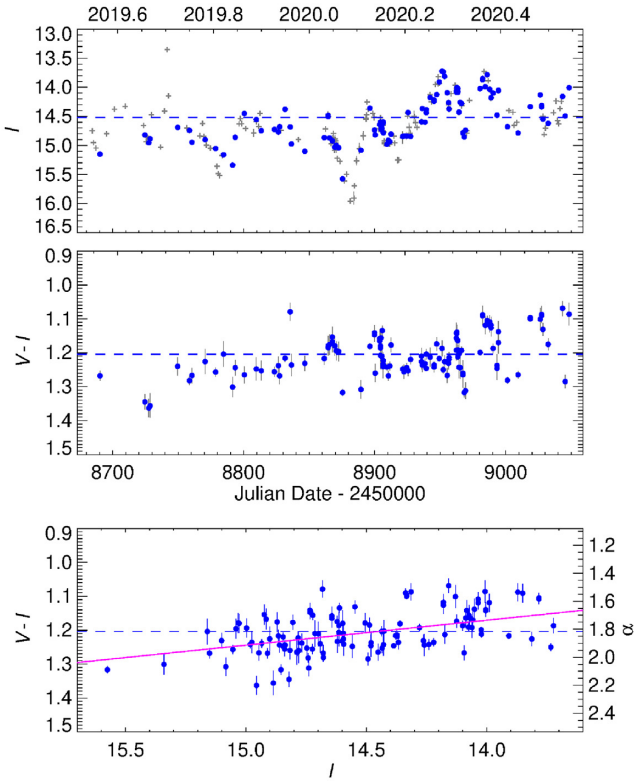


Figure 5. The top panel shows the light curve of S4 0954+65 in the I band already displayed in Fig. 3 (grey plus signs). The blue dots highlight those points used to build the $V - I$ colour indices, which are plotted in the middle panel as a function of time and in the bottom panel as a function of brightness. The horizontal dashed lines indicate average values. The linear fit (magenta line) in the bottom panel suggests a mild bluer-when-brighter trend. The α parameter on the right is the optical spectral index of the $F_{\nu} \propto \nu^{-\alpha}$ law derived from the $V - I$ colour.

5 RADIO OBSERVATIONS BY THE WEBT

Radio data from 4.8 to 37 GHz were obtained with four telescopes (see Table 1) and reduced with standard procedures (Teräsraanta et al. 1998; Giroletti & Righini 2020). The 86 and 230 GHz data were acquired under the POLAMI (Polarimetric Monitoring of AGN at Millimetre Wavelengths) Program⁹ (Agudo et al. 2018a,b; Thum et al. 2018). The reduction and calibration of the POLAMI data are described in detail in Agudo et al. (2010, 2014, 2018b). Fig. 6 compares the radio flux densities with the composite R -band flux-density optical light curve. The optical magnitudes have been converted into dereddened flux densities as explained in Section 4.

The radio flux density tends to increase with frequency, implying an inverted spectrum, with turning point around 86 GHz. Average values are 1.0, 1.1, 1.6, 1.6, and 1.2 Jy at 4.8, 8.5, 37, 86, and 230 GHz, respectively. In the same bands, the variability amplitude ($F_{\max} - F_{\min}$)/ F_{mean} is 41 per cent, 64 per cent, 83 per cent, 35 per cent, and 49 per cent. By considering that very uncertain data may artificially increase flux variability, we can rather calculate the fractional variability $f_{\text{var}} = \sqrt{(\sigma^2 - \delta^2)}/F_{\text{mean}}$, where σ^2 is the flux variance and δ^2 is the mean square error (e.g. Vaughan et al. 2003). We then obtain 10 per cent, 12 per cent, 22 per cent, 11 per cent, and 19 per cent at 4.8, 8.5, 37, 86, and 230 GHz, respectively. In both cases, flux variations

⁹<http://polami.iaa.es>

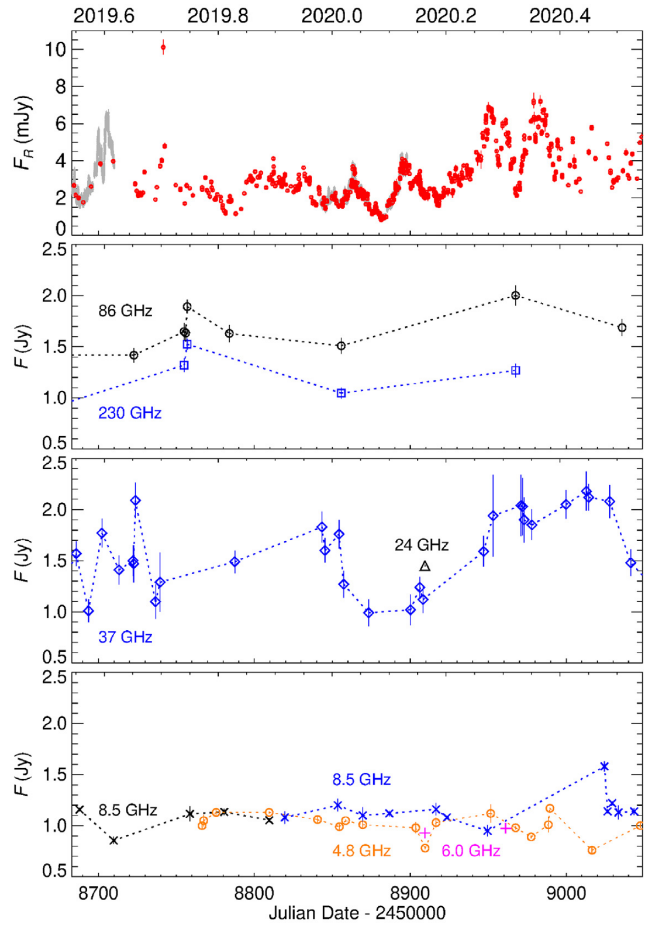


Figure 6. Dereddened WEBT (red dots) and *TESS* (grey dots) flux densities in the R band, compared to radio light curves at various frequencies, decreasing from top to bottom. Different symbols and colours distinguish different observatories and bands, as listed in Table 1.

result much stronger at 37 GHz, which however is the best-sampled light curve. For comparison, the fractional variability of the R -band flux densities is ~ 47 per cent.

In the 37 GHz light curve we notice a large dip around 2020.1, at the same time of the, more rapid, optical dimming. Whether the radio and optical events are physically linked or not is difficult to assess.

One method that is commonly used to study the correlation between two unevenly sampled time series is the discrete-correlation function (DCF Edelson & Krolik 1988; Hufnagel & Bregman 1992). Peaks in the DCF represent correlations, whose significance increases as the DCF value of the peaks approaches or even overcomes unity. The DCF cross-correlation between the composite WEBT and *TESS* flux-density light curve of S4 0954+65 and its 37 GHz flux densities is shown in Fig. 7. The main peak occurs at a time lag $\tau = 21$ d, which indicates a delay of about 3 weeks of the 37 GHz radio variations after the optical ones. To check the uncertainty on this time delay, we ran 2000 flux randomization/random subset selection (FR/RSS) Monte Carlo simulations (Peterson et al. 1998; Raiteri et al. 2003). For each of the resulting DCFs, we calculated the centroid of the peak. Fig. 7 shows the centroid distribution: 71 per cent ($\gtrsim 1\sigma$) of the simulations resulted in a time lag lying in the interval 18–24 d. A radio delay of several days or weeks is often found in blazars and has been interpreted as an indication that the radio emission comes from

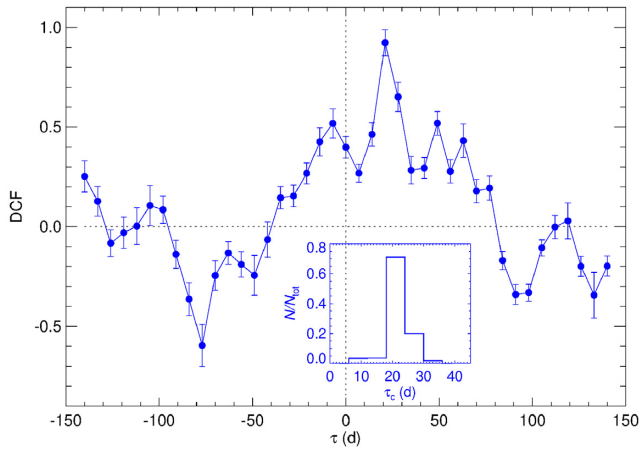


Figure 7. DCF between the composite WEBT + *TESS* flux-density light curve and the radio flux densities at 37 GHz. Optical data have been preliminarily averaged over 12 h bins, while the DCF has a 7 d resolution. The inset shows the distribution of the centroids of the DCF peaks obtained through 2000 FR/RSS Monte Carlo simulations.

a jet region which is located downstream of the optical emission zone (e.g. Raiteri et al. 2017b).

6 POLARIZATION

Blazar synchrotron emission is polarized and both the degree of optical polarization P and the electric vector polarization angle EVPA are extremely variable (e.g. Smith 1996; Marscher 2014). In particular, wide rotations of the EVPA are often observed (e.g. Marscher et al. 2008; Blinov et al. 2015, 2016, 2018; Hagen-Thorn et al. 2015; Gupta et al. 2017; Lyutikov & Kravchenko 2017; Raiteri et al. 2017a; Zhang et al. 2020).

During the time span covered in this paper, polarization observations of S4 0954+65 in the optical band were done at the Crimean (70 and 260 cm telescopes), Perkins, San Pedro Martir, and St. Petersburg observatories. The results are shown in Fig. 8 and compared with the R -band composite light curve built with WEBT and *TESS* data. The value of P_{opt} ranges between 1.7 per cent and about 29 per cent with continuous oscillations, which do not seem to be correlated with flux. This is more clearly displayed in Fig. 9, where P_{opt} is plotted versus the flux density.

The polarization angle has a more regular oscillating behaviour. If we trace the average trend of both the polarization degree and angle with a cubic spline interpolation on the 30-d binned P_{opt} and EVPA_{opt} , we can see that the EVPA_{opt} inverts its way of rotation when P_{opt} reaches a maximum or a minimum. However, the irregular sampling does not allow any clear conclusion.

In Fig. 8 we also plotted the radio polarization degree and angle at millimetre wavelengths. The values of P_{radio} and $\text{EVPA}_{\text{radio}}$ at 230 and 86 GHz are mostly in agreement. In comparison to what happens in the optical band, the radio polarization degree and angle seem much less variable. However, this could be an effect of the sparser sampling. The mean polarization angles are similar in the two bands, around 140° .

7 SHORT-TERM VARIABILITY ANALYSIS

In this section, we explore the short-term variability of the source using the exceptionally well-sampled *TESS* light curves to see whether characteristic variability time-scales can be identified.

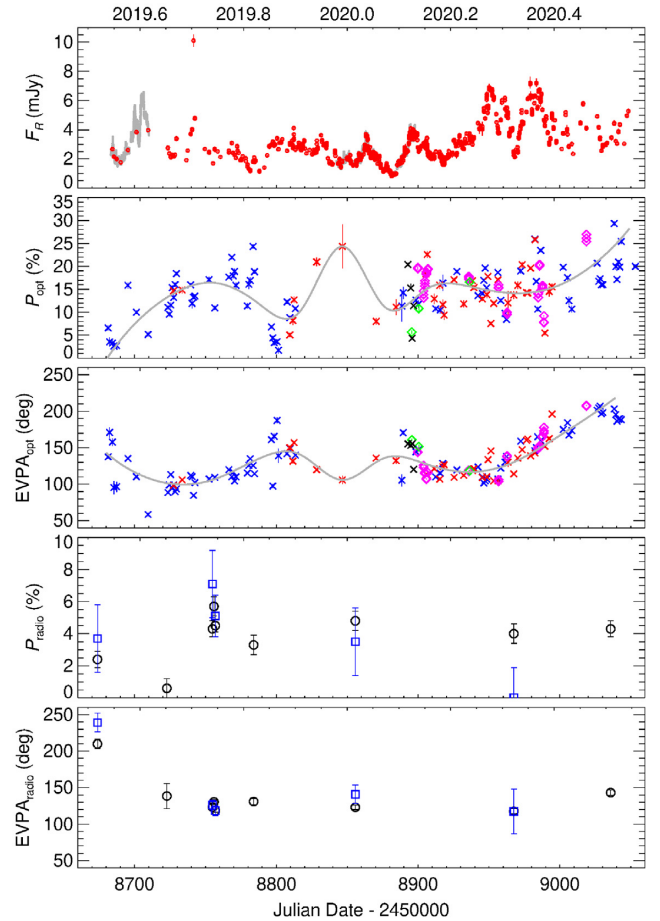


Figure 8. From top to bottom: (a) Dereddened WEBT (red dots) and *TESS* (grey dots) flux densities in the R band. (b) Degree of optical polarization. (c) Optical EVPA. (d) Degree of radio polarization at mm wavelengths. (e) Radio EVPA. In the last four panels, the various data sets are distinguished with different symbols and colours, according to Table 1. The grey solid lines in panels (b) and (c) represent cubic spline interpolations on the 30-d binned data to better follow the general trend.

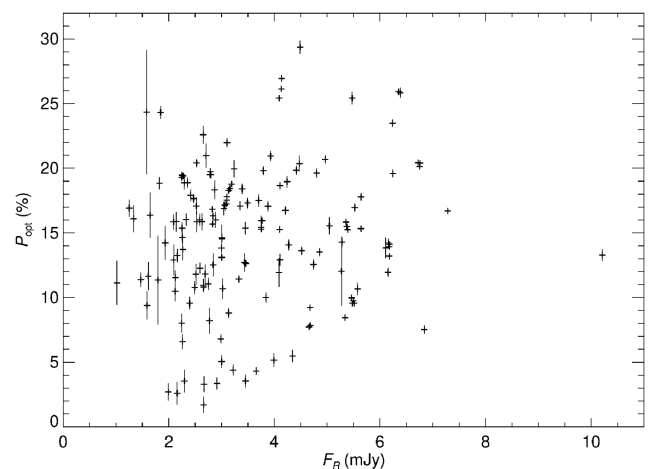


Figure 9. The degree of optical polarization P_{opt} versus the dereddened flux density in the R band, F_R , showing that there is no clear correlation between these two variables.

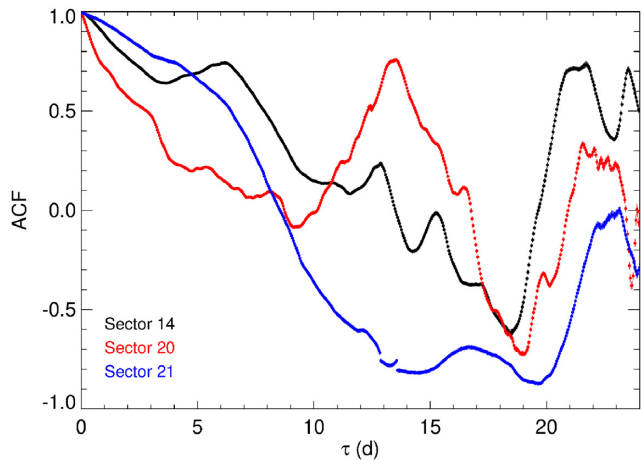


Figure 10. Autocorrelation function of the *TESS* light curve in Sector 14 (black), Sector 20 (red), and Sector 21 (blue). The ACF is binned in 1 h time lag intervals.

7.1 Autocorrelation function

When the DCF introduced in Section 5 is used to cross-correlate a light curve with itself, its autocorrelation function ACF is obtained. This is symmetric around the zero time lag, where it has a peak. Variability time-scales, i.e. distances between minima and maxima in the light curve, appear as minima in the ACF, while periodicities (or quasi-periodicities) will give rise to (approximately) equally spaced ACF maxima.

The 2 min-cadence observations by *TESS* along three time spans of almost 1 month each allow us to analyse in detail the optical variability of S4 0954+65 on time-scales from about 1 h to a few weeks. In Fig. 10 we show the ACF for the *TESS* light curve in each of the observing sectors, binned in 1 h time lag intervals. The behaviour appears quite different in the three sectors. Moreover, the signature of the shortest variability time-scales is overwhelmed by that of the long-term trend.

Therefore, to analyse the short-term variability of the *TESS* fluxes, we apply the detrending method developed by Raiteri et al. (2021). The method originates from the principle that in order to unveil the shortest variability time-scales one needs to correct for the long-term trend first. Because the boundary between long- and short-term variability is somewhat undefined, the idea is to correct the light curve for long-term trends with progressively higher time resolution to see what variability time-scales can be uncovered. Following this line, we first bin separately the Sector 14, 20, and 21 light curves, using for each of them time bins going from 7200 min (5 d) to 87 min, in 25 steps equally spaced in logarithm. We then interpolate cubic splines through the 25 binned light curves of each sector. These splines represent long-term trends with different time resolutions. We stress that when we speak of the time resolution of a given long-term trend, we mean the time interval used to bin the *TESS* light curve whose cubic spline interpolation represents the long-term trend itself.

By dividing the *TESS* fluxes by the splines (and multiplying by a constant value), detrended light curves are finally obtained, 25 for each sector. Figs 11–13 show the *TESS* fluxes in each of the three sectors, together with their 25 cubic spline interpolations representing long-term trends with progressively higher time resolution, and the corresponding detrended light curves, properly scaled. These display a variation amplitude that decreases with increasing time resolution of the long-term trend, i.e. as the spline enters the bends of the *TESS* light curve more deeply and thus reproduces it in more details. The

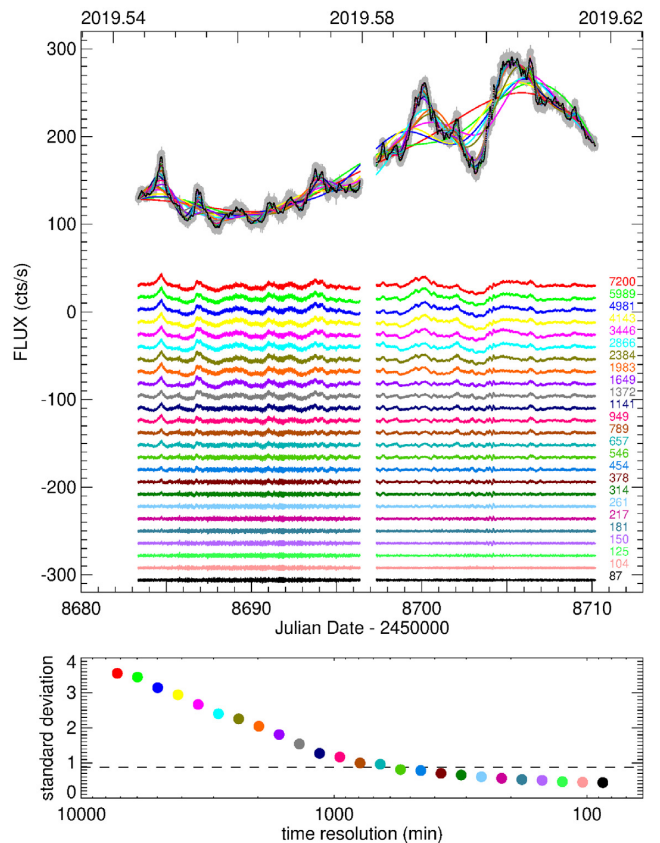


Figure 11. The top panel displays the *TESS* light curve (grey) in Sector 14. Coloured cubic spline interpolations, representing long-term trends with different time resolution between 7200 min (red) to 87 min (black), are superimposed to it. The detrended light curves obtained by dividing the *TESS* light curve by the splines are shown with the same colours, highlighting how the variability amplitude decreases with increasing long-term trend time resolution. This is better shown in the bottom panel, where the standard deviation of the detrended light curve is plotted versus the long-term resolution, i.e. the time bin used to obtain the long-term trend through cubic spline interpolation of the *TESS* binned light curve. The dashed horizontal line marks the mean error of the detrended light curves.

figure also quantifies this by showing the standard deviation of the detrended light curves versus the time resolution of the long-term trend used to obtain them. The mean error of the detrended light curves is 0.9 cts s^{-1} in Sectors 14 and 20, and it is 1.0 cts s^{-1} in Sector 21. Detrended light curves obtained from time bins shorter than about 600 min in Sectors 14 and 20, and about 1000 min in Sector 21, have standard deviation smaller than the mean error. However, well-defined flux variations can still be recognized in these detrended light curves, suggesting that they are real flux changes.

The ACFs obtained from the detrended light curves in each sector are shown in Figs 14–16 for time lags shorter than 10 d. For each sector, ACF minima are visible at various time lags. However, some of them concentrate at approximately the same τ , meaning that they do not depend on the spline resolution used to remove the long-term trend. Therefore, these minima can be considered reliable variability time-scales of the source. Similarly, there are ACF maxima at roughly the same τ , which may indicate possible quasi-periodicities. To identify the most significant signals, we found the position of the minima and maxima of each ACF by imposing limits to the first and second derivatives. Moreover, for each ACF we only considered those minima/maxima whose ACF values are smaller/larger than certain

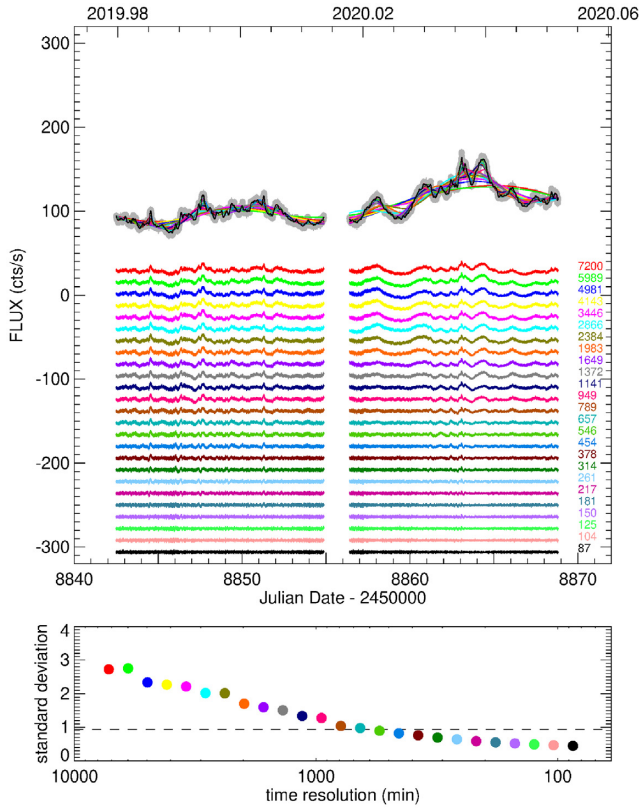


Figure 12. As in Fig. 11, but for Sector 20.

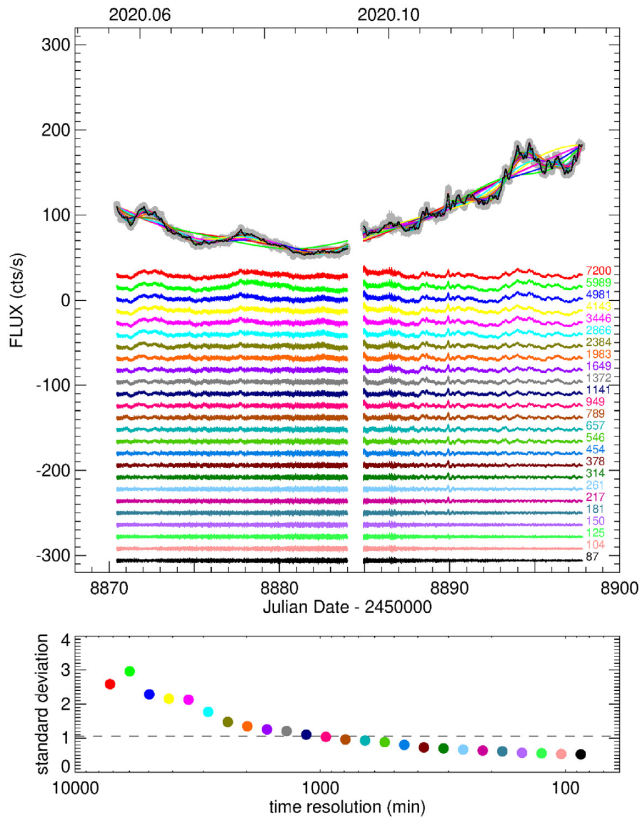


Figure 13. As in Fig. 11, but for Sector 21.

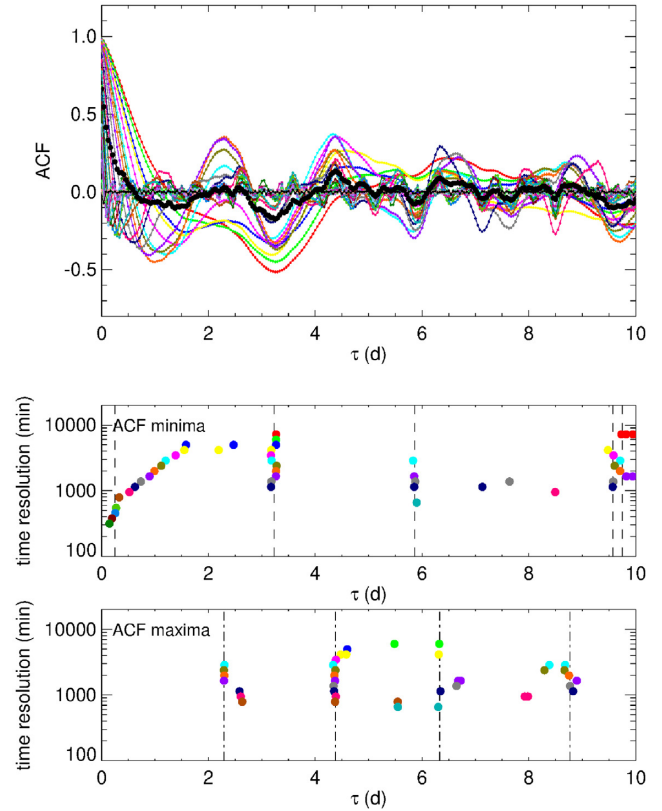


Figure 14. Top panel: the ACFs of the detrended light curves of Sector 14 shown in Fig. 11. The black dots represent the average ACF, whose minimum and second maximum are used as thresholds for the significance of the minima/maxima of the single ACFs. Middle/Bottom panel: the time lag of the most significant ACF minima/maxima versus the time resolution of the spline used to perform the detrending. The vertical lines mark the results of the weighted means on the most significant signals. They are also reported in Table 2. In the bottom panel, we do not show the absolute maxima at the origin.

thresholds. These were fixed by calculating an average ACF and using its minimum as the threshold for the single ACF minima, and its second maximum (besides that in the origin) as a threshold for the single ACF maxima. The thresholds for the minima were thus set to -0.175 , -0.139 , and -0.164 for Sectors 14, 20, and 21, respectively. The corresponding thresholds for the maxima were 0.133 , 0.125 , and 0.107 . We then performed a weighted mean of the closest signals, with weights proportional to their ACF values and finally selected the minima and maxima that show up more frequently in the ACFs of a given sector, i.e. with more than three elements contributing to the mean. The time lags of the minima represent the most significant variability time-scales, while those of the roughly equally spaced maxima represent possible quasi-periodicities. The time lags of the significant minima and maxima are reported in Table 2 for each sector.

We adopted the same detrending method, but using the structure function SF (Simonetti, Cordes & Heeschen 1985) instead of the ACF, to check the results reported in Table 2. This analysis is detailed in the Appendix and confirms the above findings, with the addition of possible further characteristic variability time-scales.

We note the interesting sequence of ACF maxima at 2.3, 4.4, 6.3, and 8.8 d in Sector 14, the sequence 3.1, 6.6, and 9.9 d in Sector 20, and the sequence 2.7, 5.3, and 8.0 d in Sector 21. These sequences may indicate quasi-periodicities, which will be further investigated with the periodogram in the next section.

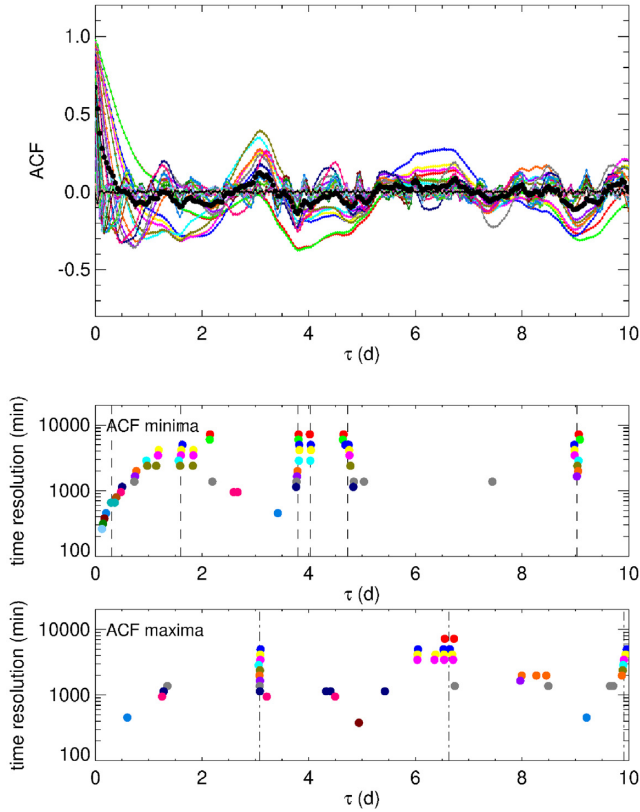


Figure 15. As in Fig. 14, but for Sector 20.

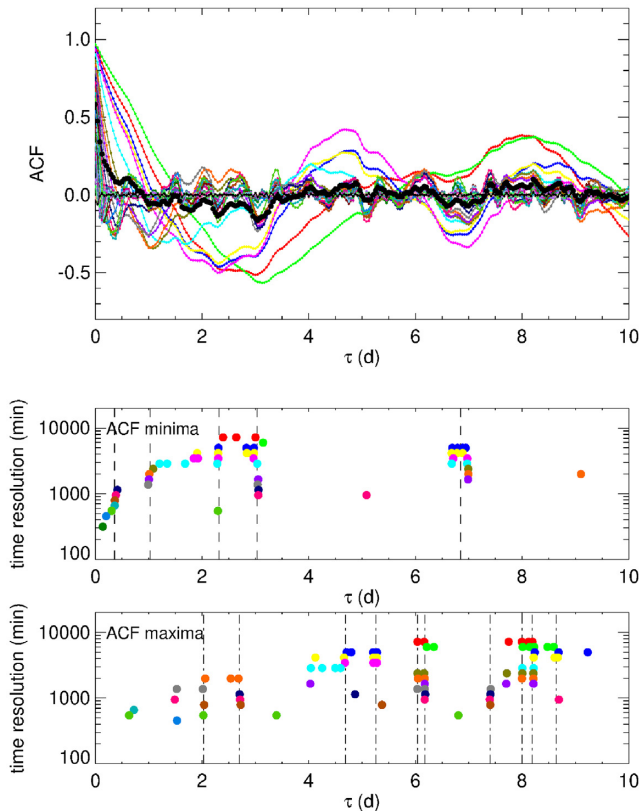


Figure 16. As in Fig. 14, but for Sector 21.

In any case, the source short-term variability appears strongly unstable, with multiple time-scales from a few hours to a few days, which change from time to time.

7.2 Periodogram

As mentioned earlier, the nearly equally spaced ACF significant maxima derived in Section 7.1 and whose time lags are reported in Table 2 may indicate possible periodic patterns in the source variability. The reliability of them can be checked with the periodogram, which is an estimate of the power spectral density (PSD).¹⁰ Fig. 17 shows the PSD of the *TESS* light curves in the three sectors, obtained with the normalized Lomb–Scargle periodogram (Scargle 1982; Horne & Baliunas 1986, see also Raiteri et al. 2021). They have been computed in the frequency range $\sim 4 \times 10^{-7}$ to $\sim 1.67 \times 10^{-3}$ Hz, the first limit corresponding to the duration of the light curve and the second to 10 min, which is the width of the light curve bins (see Section 2). Indeed, at this frequency the PSDs show a clear spike. Because of the frequency sampling, the PSDs are better sampled at the highest frequencies, where they show a flattening, i.e. a white noise behaviour. We thus binned the PSDs in steps of $\log f = 0.1$ [Hz] and used linear regression with χ^2 error statistic minimization to fit them with a broken power law up to the Nyquist frequency,¹¹ with slope fixed to zero after the break frequency. The breaks occur at $\log f = -3.77 \pm 0.24$, -3.70 ± 0.27 , -3.61 ± 0.30 [Hz] for Sector 14, 20 and 21, respectively (corresponding to ~ 5888 , 5012, and 4074 s), while the slopes of the power law before the break are -2.32 ± 0.30 , -2.07 ± 0.28 , -1.98 ± 0.26 , with significance levels of the Kolmogorov–Smirnov statistic of 0.936 in Sectors 14 and 20, and 0.997 in Sector 21. This confirms the red noise nature of the source variability up to frequencies corresponding approximately to 1–1.5 h, while for higher frequencies white noise dominates.

PSDs sampled in time for the three sectors are displayed in Fig. 18. Significance levels of 95, 99, and 99.9 per cent are calculated as in Raiteri et al. (2021), following the prescriptions given by Vaughan (2005). A zoom into the 0.3–2 d period range is shown in Fig. 19. None of the PSD peaks exceeds the 99.9 per cent significance level, while there are a few signals in Sectors 14 and 20 that overcome the 99 per cent level. These are reported in Table 2, where they can be compared with the results obtained from the time-series analysis by means of the ACF. The comparison shows that there are no common values, i.e. there is no repeated time distance between the light curve peaks or dips that correspond to the period of sinusoidal components. The reason may be that we are in the presence of quasi-periodic signals, so that the power density is spread over different times, becoming weaker (Vaughan 2005). In any case, we cannot conclude in favour of short-term periodicities in the S4 0954+65 optical light curves.

We finally note that the marginally significant signal at 0.62 d present in Sector 20 is also visible in the ACF maxima of Sectors 20 and 21 (see Figs 15 and 16) and in the SF minima of Sector 20 (see Fig. A2), thus representing an interesting recurrence. Moreover, in all sectors there is a significant ACF minimum at a time lag about one-half of this signal (and similar values are found in the SF maxima in the appendix).

¹⁰In the following, we will use the term ‘PSD’ as a synonym of ‘periodogram’, as is commonly used.

¹¹The Nyquist critical frequency is defined as $f_c = N/(2\Delta T)$, where N is the number of data points in the time interval ΔT .

Table 2. Results of the time-series analysis on the *TESS* light curves in Sectors 14, 20, 21, and the whole composite optical light curve. The tabulated τ values derived from the ACF on the detrended *TESS* light curves are obtained as weighted means of the most recurrent signals; the numbers in brackets indicate the number of elements contributing to the corresponding weighted mean.

<i>TESS light curves</i>	
Sector	τ of ACF minima (d)
14	0.25 (5), 3.23 (11), 5.86 (5), 9.57 (5), 9.75 (5)
20	0.31 (9), 1.60 (5), 3.80 (9), 4.03 (4), 4.73 (9), 9.03 (9)
21	0.36 (5), 1.03 (4), 2.32 (6), 3.03 (10), 6.85 (14)
Sector	τ of ACF maxima (d)
14	2.29 (4), 4.38 (10), 6.33 (4), 8.77 (6)
20	3.08 (9), 6.63 (9), 9.91 (6)
21	2.03 (4), 2.70 (4), 4.69 (7), 5.26 (7), 6.04 (4), 6.18 (8), 7.40 (4), 8.00 (5), 8.19 (10), 8.64 (5)
Sector	PSD peaks (d) with period ≥ 0.5 d
14	0.90
20	0.62, 1.10, 1.39
21	–
<i>Composite light curve</i>	
τ of ACF minima (d)	18, 73, 105, 139, 173
τ of ACF maxima (d)	33, 91, 154, 190–193
PSD peaks (d)	31, 39.7

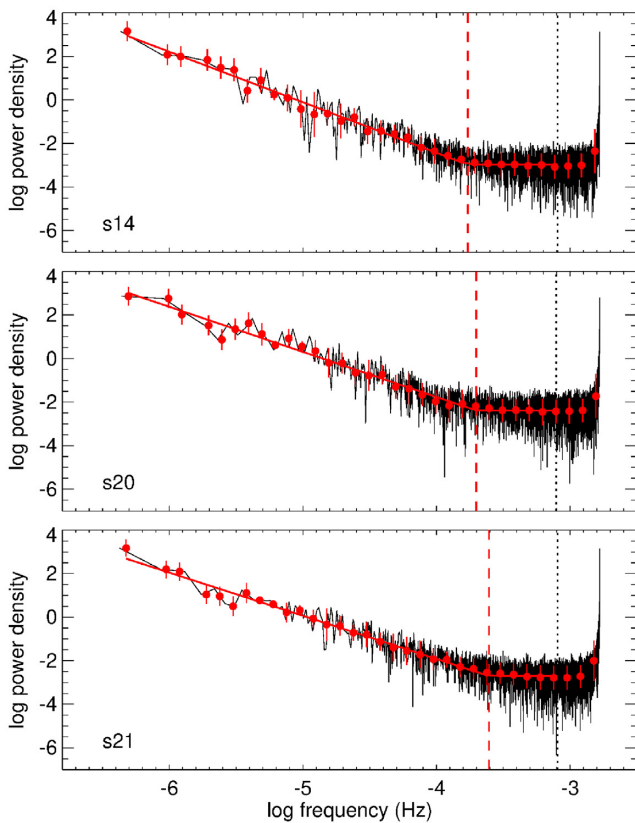


Figure 17. Frequency-sampled PSD computed on the *TESS* light curves in the three sectors. The dotted vertical lines mark the Nyquist frequency. The solid red lines represent a broken power-law fit to the PSD, binned in steps of $\log f = 0.1$ up to the Nyquist frequency. The vertical dashed red lines indicate the best-fitting break frequency.

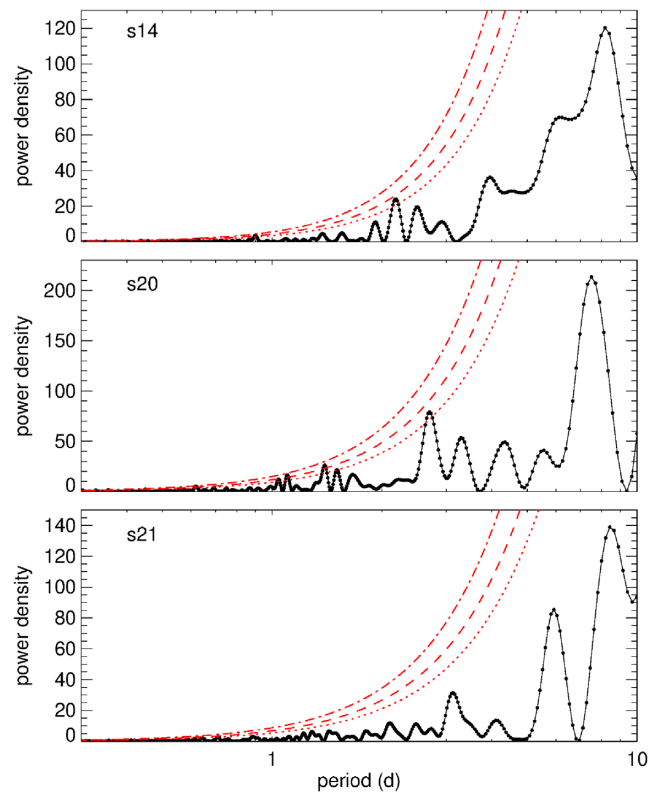


Figure 18. Time-sampled periodogram computed on the *TESS* light curves in the three sectors. The dotted, dashed, and dot-dashed red lines indicate the significance levels of 95, 99, and 99.9 per cent, respectively.

8 LONG-TERM VARIABILITY ANALYSIS

To investigate the presence of characteristic variability time-scales during the whole period analysed in this paper, we use the composite light curve including the WEBT data together with the *TESS* data stretched to match the WEBT ones (see Section 3). This is shown

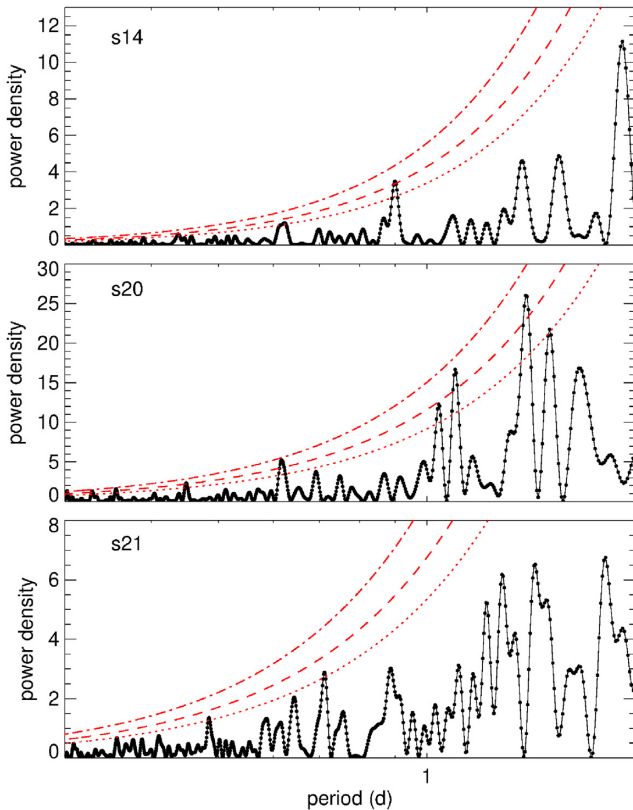


Figure 19. A zoom of Fig. 18 into the 0.3–2 d period range.

again in Fig. 20, where the main flares have been numbered. They come in pairs, whose peaks are separated by an approximately 1 month time interval. This is true for the pairs 1-2, 3-4, and 5-6.

The ACF of the composite light curve is plotted in Fig. 20 and shows many signals, corresponding to the cross-correlation between different light-curve peaks (and dips). In particular, the first maximum at about 1 month corresponds to the coupling of the 1-2, 3-4, and 5-6 pairs. The positions of the subsequent ACF maxima are roughly multiples of this time interval. The signals are produced by the pairs indicated in the figure. This suggests the presence of a quasi-periodicity of roughly 1 month.

The result of the periodogram analysis on the composite light curve is shown in Fig. 21 and confirms the quasi-periodicity of about 1 month found with the ACF. Indeed, a strong signal with significance level greater than 99.9 per cent is visible at 31.2 d. The fact that the two methods converge on the same result suggests that it is reliable and that there is a mechanism causing recurrent variations on a roughly monthly period. The Deeming spectral window (Deeming 1975) does not show any pathology in the data distribution at the frequency corresponding to this signal. In Fig. 20 we plot a sinusoidal function with the above period, to be compared with the general trend of the light curve. The agreement is fair, though the occurrence of the observed flares is sometimes slightly shifted with respect to the analysis prediction, indicating that we must rather speak of quasi-periodicity.

9 MODELLING THE LONG-TERM OPTICAL LIGHT CURVE

Quasi-periodicities in blazar light curves have been claimed several times (e.g. Sillanpaa et al. 1988, 1996; Lainela et al. 1999; Raiteri

et al. 2001; Ackermann et al. 2015; Sandrinelli et al. 2017; Otero-Santos et al. 2020) and have been explained in terms of jet precession or orbital motion in a binary system of supermassive black holes, often involving a helical jet (e.g. Villata et al. 1998; Ostorero, Villata & Raiteri 2004; Rieger 2004; Valtonen & Pihajoki 2013; Sobacchi, Sormani & Stamerra 2017).

Many observations suggest that blazar jets can have a bending, helical or twisted structure (McHardy et al. 1990; Conway & Wrobel 1995; Britzen et al. 2005; Perucho et al. 2012; Fromm et al. 2013; Larionov et al. 2013; Britzen et al. 2017). Magnetohydrodynamical simulations in 3D show that jet wiggling can result from kink instabilities or other mechanisms (Nakamura, Uchida & Hirose 2001; Moll, Spruit & Obergaulinger 2008; Mignone et al. 2010; Liska et al. 2018). A helical jet model was developed by Villata & Raiteri (1999) to explain the spectral variability of Mkn 501 and later applied to interpret the multiwavelength behaviour of other blazars (Raiteri et al. 1999, 2009). In particular, in Ostorero, Villata & Raiteri (2004) the rotation of the helical jet, possibly driven by orbital motion, was able to explain the 5.7 yr quasi-periodicity of AO 0235+164 found by Raiteri et al. (2001).

In agreement with the above studies, we adopt a model where the relativistic emitting plasma continuously flows along the helical structure with a constant bulk Lorentz factor Γ . The jet is inhomogeneous in the sense that any portion of it, at its fixed distance from the jet apex, emits a constant flux in a given frequency band. This is determined by the local physical properties, such as magnetic field, plasma density, and optical depth. The higher the synchrotron frequencies emitted, the closer to the jet apex are the corresponding emitting regions. X-rays,¹² ultraviolet, optical, infrared, micro and mm waves, radio waves at longer and longer wavelengths are thus produced at increasing distances from the central engine, and along more and more elongated (and consequently more curved) regions downstream the jet. All these jet properties are assumed to remain constant in time, apart from the rotation of the helical structure, which is the only source of observed variability at any frequency. As the helix rotates, every emitting region will change its orientation with respect to the line of sight and this will produce a variation of the observed flux. Indeed, because of relativistic boosting, the observed flux density F_ν is enhanced with respect to the rest-frame flux density F'_ν by some power of the Doppler factor δ . In a continuous jet (e.g. Urry & Padovani 1995):

$$F_\nu(\nu) = \delta^{2+\alpha} F'_\nu(\nu), \quad (1)$$

where α is the index of the intrinsic, power-law spectrum, and

$$\delta = [\Gamma(1 - \beta \cos \theta)]^{-1}. \quad (2)$$

Therefore, the flux density depends on the Doppler factor, which in turn depends on both the viewing angle θ and the Lorentz factor $\Gamma = (1 - \beta^2)^{-1/2}$, where β is the plasma bulk velocity in units of the speed of light. As a consequence, in a twisting jet, the source is observed in a flaring state at a given frequency every time the corresponding jet emitting region becomes closely aligned with the line of sight, causing an increase of the Doppler factor. In our model, higher frequencies are coming from jet regions much shorter than the helix pitch and they show larger amplitude variability because they undergo strong and rapid orientation changes. Lower frequencies, e.g. radio waves, are emitted from more extended regions, possibly covering several helix pitches, and their flux variations are much

¹²Significant X-ray synchrotron emission is expected only in high-energy peaked BL Lacs, which is not the case of S4 0954+65.

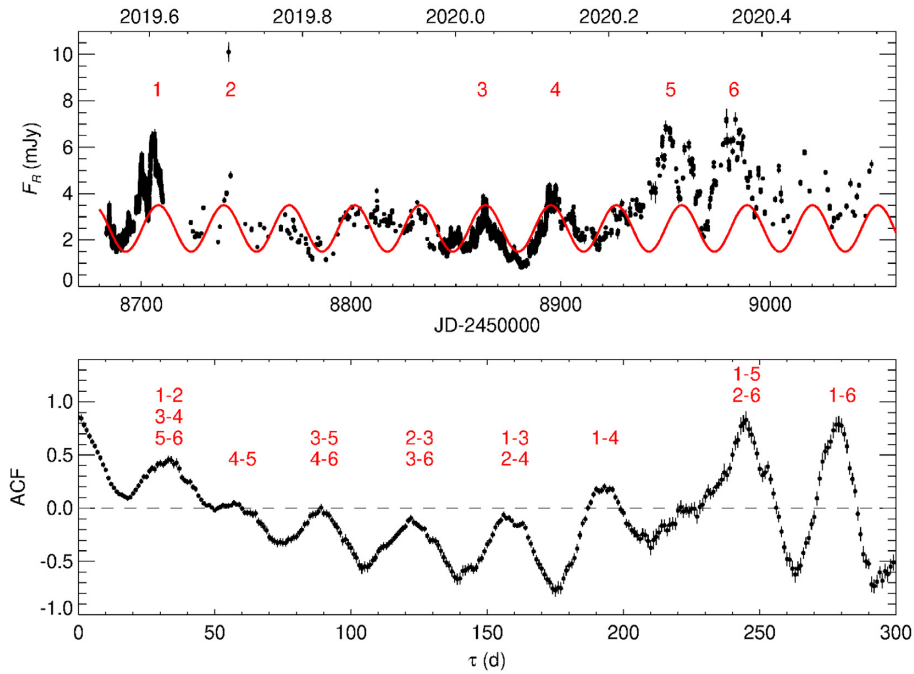


Figure 20. Top: the black dots represent the composite light curve obtained by including both the WEBT data and the *TESS* data stretched to match the WEBT ones. The red numbers mark the main flares. The red solid line is a sinusoidal function with period of 31.2 d, as found by the PSD analysis. Bottom: the ACF on the composite light curve (black). Data points have preliminary been binned over 6 h, while the ACF resolution is 1 d. The red labels over the ACF maxima indicate the pairs of light curve peaks that are mainly responsible for them.

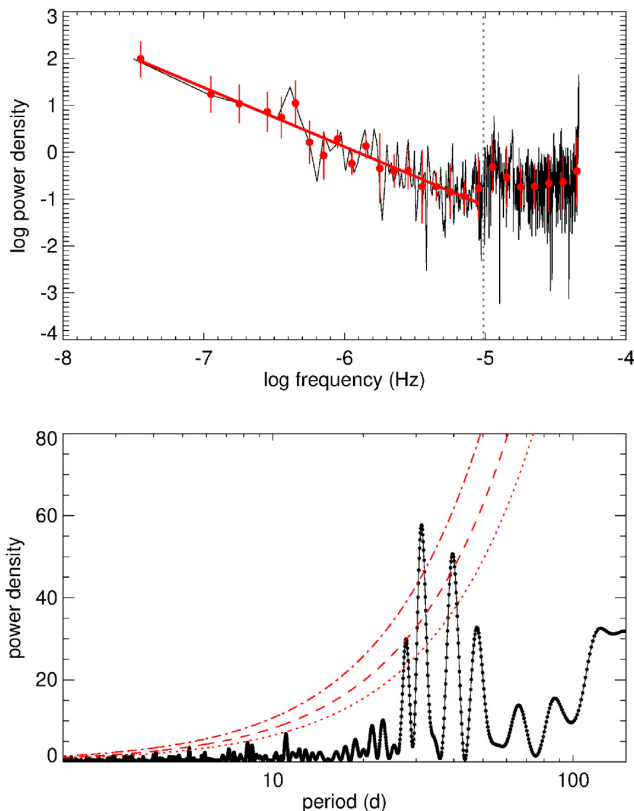


Figure 21. Top: Periodogram of the composite WEBT + *TESS* 6-h binned light curve sampled in frequency. Bottom: Periodogram of the same composite light curve sampled in period.

smoother and slower. In this context, we assume that the region emitting the optical radiation of S4 0954+65 is located in a helical jet, whose rotation produces the 31.2 d quasi-periodicity found in the previous section. This optical emitting region must still be much shorter than the helical pitch, and so has a very small curvature, and consequently shows strong and rapid variability as the helix rotates and its viewing angle changes.

In the rotating helical jet scenario, $\theta(t)$ of a given emitting region depends on the helix pitch angle ζ and on the angle between the helix axis and the line of sight ψ according to

$$\cos \theta(t) = \cos \psi \cos \zeta + \sin \psi \sin \zeta \cos \phi(t). \quad (3)$$

The angle $\phi(t)$ is the variable azimuthal difference between the line of sight and the direction of the bulk plasma velocity in the considered jet region, and contains the information on the periodicity: $\phi(t) = \omega(t - t_0) = 2\pi(t - t_0)/T$, being T the period and t_0 the time of one of the periodic peaks in the observed light curve. From equation 3 we can calculate $\theta(t)$ once ψ and ζ are set. We fix $\psi = 1^\circ$ and consider a toy model where ζ is fixed to 4° . As shown in Fig. 22, the result is a periodic variation of $\theta(t)$. From $\theta(t)$, and adopting $\Gamma = 10$, we calculate $\delta(t)$ with equation 2 and then the long-term trend predicted by the toy model from equation 1. This is plotted in Fig. 22 (with $\alpha = 1.82$ as found in Section 4 from the colour analysis) and shows a general agreement with the observed flux-density behaviour, but cannot reproduce in particular the difference in flare amplitudes.

The fact that the observed flux variations do not appear as perfectly periodic, identical, and symmetric outbursts implies that the toy model is an oversimplification and that the helical pattern cannot be a perfect and rigid structure. Indeed, we can expect at least some oscillations around its equilibrium configuration. The rotation of the jet structure drives the jet helical pattern and tends to create a stronger and stronger toroidal magnetic field component as the helix becomes more twisted. The tension of these magnetic field

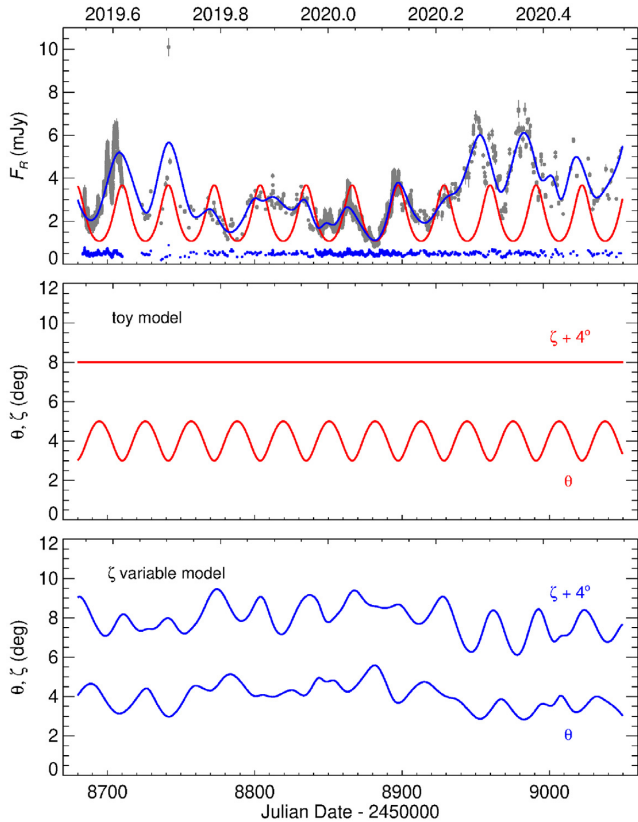


Figure 22. Top: The optical light curve of S4 0954+65 (grey points) with long-term trends overlapped. The red line refers to the toy model with pitch angle ζ fixed to 4° . The blue line is a cubic spline interpolation through the 7-d binned light curve and also represents the final result of the model with variable ζ . Middle: The periodic behaviour of the viewing angle θ obtained with the toy model. Bottom: the angles θ and ζ resulting from the model with variable ζ that produce the long-term trend shown in blue in the top panel. Correction of the observed flux densities for the variable Doppler boosting produces the ‘residual’ fluxes shown in the top panel (blue points).

lines is what collimates the jet and prevents its inflation because of the centrifugal force pushing the helically moving plasma outwards. This force, added to the various (material and magnetic) pressures acting in the jet, must be in equilibrium with the toroidal magnetic tension.¹³ Therefore, when the helical jet becomes too twisted (larger pitch angle and stronger magnetic tension), the centrifugal force and the pressures increase too, expanding the structure towards a more relaxed morphology with a smaller pitch angle, and so on around the dynamical equilibrium configuration.

In line with the above scenario, we assume that the pitch angle ζ can change in time and calculate numerically its temporal evolution from equation 3. There $\theta(t)$ is obtained by using equations (1) and (2), where the flux long-term trend is modelled by means of a cubic-spline interpolation through the 7-d binned light curve (also shown in Fig. 22). The result is plotted in Fig. 22, where both $\zeta(t)$ and $\theta(t)$ are displayed. The predicted time behaviour of these angles is what determines the long-term trend traced by the spline interpolation in our geometrical model. The corresponding δ values vary between ~ 10 and ~ 16 .

¹³For an analytical view of helical magnetohydrodynamic equilibria see e.g. Villata & Tsinganos (1993), Villata & Tsinganos (1994), Villata & Ferrari (1994a), Villata & Ferrari (1994b), and Villata & Ferrari (1995).

Once we correct the observed flux densities for the effect of the time-dependent beaming,¹⁴ the light curve of the residual flux densities (shown in Fig. 22) is characterized by smaller fluctuations similar to those obtained from the 5-d detrending in Section 7.

We finally stress that the set of model parameters adopted here are reasonable values that are not necessarily unique, but can demonstrate the strength of the rotating helical jet scenario. However, it is remarkable that Jorstad et al. (2017) found $\Gamma = 11.4 \pm 3.1$, $\theta = 1.5^\circ \pm 0.7^\circ$ and opening angle $\sim 3.5^\circ$ for the parsec-scale radio jet of S4 0954+65.

10 CONCLUSIONS

In this paper, we have presented the results of 1-yr monitoring of S4 0954+65 by the WEBT, complemented by three periods of *TESS* observations. The source was in a state of moderate activity, with a maximum variability amplitude of ~ 2.8 mag in the *R* band. In particular, we detected an extreme variability episode, with a brightening of 1 mag in 24 h, followed by a 0.8-mag dimming in 23 h. The optical colours showed a very mild bluer-when-brighter long-term trend, while the short-term flux changes are much more chromatic, as already found, e.g. in a previous study of another BL Lac object, S5 0716+714, by Raiteri et al. (2021). The radio flux looked rather stable at long wavelengths, while it was quite variable at 37 GHz. We found a possible 3-weeks time delay of the flux variations at this frequency with respect to the optical ones.

The source also showed strong variability in both the polarization degree and electric vector polarization angle. There is no general correlation between the P_{opt} and the optical flux. However, the mean trends of P_{opt} and EVPA_{opt} suggest that the polarization angle changes the direction of rotation every time P_{opt} reaches a maximum or a minimum. Although sampled in a sparser way, the radio polarization in general shows a stabler behaviour.

We conducted a detailed analysis of the short-term flux variations occurring in the *TESS* light curves. We applied the detrending method developed by Raiteri et al. (2021), correcting the *TESS* light curves for long-term trends with progressively higher time resolution and then calculating the corresponding autocorrelation functions. ACF minima which are common to various detrended light curves are considered to indicate genuine variability time-scales, while common maxima that repeat at nearly equally spaced time intervals represent possible quasi-periodicities, whose reliability is tested with the periodogram. We found a different behaviour in the three *TESS* sectors, with multiple variability time-scales, which are confirmed also by a structure function analysis, but no trustworthy periodicity.

On the contrary, when we examine the long-term composite light curve built with WEBT and *TESS* data, we found that the main peaks (and dips) repeat with about 1 month time interval. This result is confirmed by both the ACF and periodogram analyses. Most notably, in at least two cases, we can recognize ‘twin’ flares (3-4 and 5-6 in Fig. 20) with the same flux amplitude.

We explain the long-term quasi-periodic variations of the optical light curve of S4 0954+65 in terms of an inhomogeneous helical jet that rotates and whose pitch angle varies in time because of small oscillations of the helical structure around its dynamical equilibrium configuration, which in our case is given by $\zeta \sim 4^\circ$.

In Fig. 22 we showed the residual fluxes once the long-term trend due to the variation of the Doppler factor has been removed. Their

¹⁴This correction is obtained by dividing the flux densities by the long-term trend.

fluctuations are similar to those analysed in the *TESS* light curves in Section 7. The variability time-scales of the order of a few days can be explained in terms of a stranded jet structure, as in the S5 0716+714 case studied by Raiteri et al. (2021). Their geometric nature is consistent with the almost achromatic behaviour.

Moreover, if the helical structure of the jet is composed of wrapped filaments, then the magnetic field will not follow the main helical path, but will have a more complex structure. This is consistent with the polarimetric data: in the case of a rotating helical structure of the magnetic field, we would expect to see loops of rotation (with different radii in the case of variable pitch angle) of the relative Stokes parameters in a u versus q plot, which are not observed.

On even shorter time-scales (less than one day), the strongly chromatic variability is likely intrinsic, being associated with energetic processes in the jet, like shock waves in a turbulent plasma. Indeed, the superposition of systematic (Doppler factor changes, shocks-in-jet) and stochastic (turbulence) processes can also account for the observed variations of the polarization degree and position angle (Weaver et al. 2020).

In this scenario, the smoothness and time delay of the radio emission would indicate that most of it comes from a jet region that is spatially separated (likely downstream) and wider than the optical one. In this case, the radio emission would be the result of the sum of the contributions coming from a broad continuous range of viewing angles (e.g. Raiteri et al. 2017b), so that the marking of the optical periodicity is swamped. Finally, according to this model, the radio jet components visible in the VLBI/VLBA images of this and other sources (e.g. Morozova et al. 2014; Casadio et al. 2015; Jorstad et al. 2017; Larionov et al. 2020) would be the most beamed parts of the continuous helical path (e.g. Bach et al. 2006).

ACKNOWLEDGEMENTS

We dedicate this paper to the memory of our esteemed colleague Valeri M. Larionov, who has been a WEBT pillar for 20 yr and whose loss we deeply mourn. We thank the SRT operators Elise Egron, Delphine Perrodin, and Mauro Pili for help with the observations. This paper includes data collected by the *TESS* mission. Funding for the *TESS* mission is provided by the NASA Explorer Program. Partly based on observations made with the Nordic Optical Telescope, owned in collaboration by the University of Turku and Aarhus University, and operated jointly by Aarhus University, the University of Turku and the University of Oslo, representing Denmark, Finland and Norway, the University of Iceland and Stockholm University at the Observatorio del Roque de los Muchachos, La Palma, Spain, of the Instituto de Astrofísica de Canarias. This article is partly based on observations made in the Observatorios de Canarias del IAC with the Liverpool telescope operated on the island of La Palma by the Liverpool John Moores University in the Observatorio del Roque de Los Muchachos. This article is partly based on observations made with the LCOGT Telescopes, one of whose nodes is located at the Observatorios de Canarias del IAC on the island of Tenerife in the Observatorio del Teide. This article is partly based on observations made with the IAC-80 operated on the island of Tenerife by the Instituto de Astrofísica de Canarias in the Spanish Observatorio del Teide. Many thanks are due to the IAC support astronomers and telescope operators for supporting the observations at the IAC-80 telescope. This publication makes use of data obtained at Metsähovi Radio Observatory, operated by Aalto University in Finland. This research has made use of NASA's Astrophysics Data System and of the NASA/IPAC Extragalactic Database (NED), which is operated by the Jet Propulsion Laboratory,

California Institute of Technology, under contract with the National Aeronautics and Space Administration. The research at Boston University was supported by NASA grants 80NSSC20K1566 (Fermi Guest Investigator Program) and 80NSSC21K0243 (TESS Guest Investigator Program). This study was based (in part) on observations conducted using the 1.8 m Perkins Telescope Observatory (PTO) in Arizona (USA), which is owned and operated by Boston University. GD, MS, GM, and OV acknowledge the observing grant support from the Institute of Astronomy and Rozhen NAO BAS through the bilateral joint research project 'Gaia Celestial Reference Frame (CRF) and fast variable astronomical objects' (2020–2022, leader is G.Damljanovic), and support by the Ministry of Education, Science and Technological Development of the Republic of Serbia (contract No 451-03-68/2020-14/200002) This research was partially supported by the Bulgarian National Science Fund of the Ministry of Education and Science under grants DN 18-13/2017, KP-06-H28/3 (2018), KP-06-H38/4 (2019), and KP-06-KITAJ/2 (2020). SOK acknowledges financial support by Shota Rustaveli National Science Foundation of Georgia under contract PHDF-18-354 EB acknowledges support from DGAPA-PAPIIT GRANT IN113320. This work is partly based upon observations carried out at the Observatorio Astronómico Nacional on the Sierra San Pedro Mártir (OAN- SPM), Baja California, Mexico. We acknowledge support by Bulgarian National Science Fund under grant DN18-10/2017 and National RI Roadmap Project DO1-383/18.12.2020 of the Ministry of Education and Science of the Republic of Bulgaria. IA acknowledges financial support from the Spanish 'Ministerio de Ciencia e Innovación' (MCINN) through the 'Center of Excellence Severo Ochoa' award for the Instituto de Astrofísica de Andalucía-CSIC (SEV-2017-0709). Acquisition and reduction of the POLAMI data was supported in part by MICINN through grants AYA2016-80889-P and PID2019-107847RB-C44. The POLAMI observations were carried out at the IRAM 30m Telescope. IRAM is supported by INSU/CNRS (France), MPG (Germany) and IGN (Spain).

DATA AVAILABILITY

The data collected by the WEBT collaboration are stored in the WEBT archive at the Osservatorio Astrofisico di Torino - INAF (<http://www.oato.inaf.it/blazars/webt/>); for questions regarding their availability, please contact the WEBT President Massimo Villata (massimo.villata@inaf.it).

REFERENCES

- Ackermann M. et al., 2015, *ApJ*, 813, L41
 Agarwal A. et al., 2015, *MNRAS*, 451, 3882
 Agudo I., Thum C., Wiesemeyer H., Krichbaum T. P., 2010, *ApJS*, 189, 1
 Agudo I., Thum C., Gómez J. L., Wiesemeyer H., 2014, *A&A*, 566, A59
 Agudo I., Thum C., Ramakrishnan V., Molina S. N., Casadio C., Gómez J. L., 2018a, *MNRAS*, 473, 1850
 Agudo I. et al., 2018b, *MNRAS*, 474, 1427
 Bach U. et al., 2006, *A&A*, 456, 105
 Bachev R., 2015, *MNRAS*, 451, L21
 Becerra González J., Acosta-Pulido J. A., Boschin W., Clavero R., Otero-Santos J., Carballo-Bello J. A., Domínguez-Palmero L., 2021, *MNRAS*, preprint ([arXiv:2010.14532](https://arxiv.org/abs/2010.14532))
 Bessell M. S., Castelli F., Plez B., 1998, *A&A*, 333, 231
 Blinov D. et al., 2015, *MNRAS*, 453, 1669
 Blinov D. et al., 2016, *MNRAS*, 462, 1775
 Blinov D. et al., 2018, *MNRAS*, 474, 1296
 Britzen S., Witzel A., Krichbaum T. P., Beckert T., Campbell R. M., Schalinski C., Campbell J., 2005, *MNRAS*, 362, 966

- Britzen S. et al., 2017, *A&A*, 602, A29
 Carnerero M. I. et al., 2015, *MNRAS*, 450, 2677
 Carnerero M. I. et al., 2017, *MNRAS*, 472, 3789
 Casadio C. et al., 2015, *ApJ*, 813, 51
 Cheng X.-L., Zhang Y.-H., Xu L., 2013, *MNRAS*, 429, 2773
 Conway J. E., Wrobel J. M., 1995, *ApJ*, 439, 98
 Deeming T. J., 1975, *Ap&SS*, 36, 137
 Edelson R. A., Krolik J. H., 1988, *ApJ*, 333, 646
 Fromm C. M., Ros E., Perucho M., Savolainen T., Mimica P., Kadler M., Lobanov A. P., Zensus J. A., 2013, *A&A*, 557, A105
 Giroletti M., Righini S., 2020, *MNRAS*, 492, 2807
 Gupta A. C. et al., 2017, *MNRAS*, 472, 788
 Hagen-Thorn V. A. et al., 2015, *Astron. Rep.*, 59, 551
 Heidt J., Wagner S. J., 1996, *A&A*, 305, 42
 Horne J. H., Baliunas S. L., 1986, *ApJ*, 302, 757
 Hufnagel B. R., Bregman J. N., 1992, *ApJ*, 386, 473
 Jorstad S. G. et al., 2017, *ApJ*, 846, 98
 Lainera M. et al., 1999, *ApJ*, 521, 561
 Landoni M., Falomo R., Treves A., Scarpa R., Reverte Payá D., 2015, *AJ*, 150, 181
 Larionov V. M., Villata M., Raiteri C. M., 2010, *A&A*, 510, A93
 Larionov V. M. et al., 2013, *ApJ*, 768, 40
 Larionov V. M. et al., 2016, *MNRAS*, 461, 3047
 Larionov V. M. et al., 2020, *MNRAS*, 492, 3829
 Lawrence C. R., Pearson T. J., Readhead A. C. S., Unwin S. C., 1986, *AJ*, 91, 494
 Liska M., Hesp C., Tchekhovskoy A., Ingram A., van der Klis M., Markoff S., 2018, *MNRAS*, 474, L81
 Lyutikov M., Kravchenko E. V., 2017, *MNRAS*, 467, 3876
 MAGIC Collaboration, 2018, *A&A*, 617, A30
 Marchili N., Krichbaum T. P., Liu X., Song H. G., Gabányi K. É., Fuhrmann L., Witzel A., Zensus J. A., 2012, *A&A*, 542, A121
 Marscher A. P., 2014, *ApJ*, 780, 87
 Marscher A. P. et al., 2008, *Nature*, 452, 966
 McHardy I. M., Marscher A. P., Gear W. K., Muxlow T., Lehto H. J., Abraham R. G., 1990, *MNRAS*, 246, 305
 Mignone A., Rossi P., Bodo G., Ferrari A., Massaglia S., 2010, *MNRAS*, 402, 7
 Moll R., Spruit H. C., Obergaulinger M., 2008, *A&A*, 492, 621
 Morozova D. A. et al., 2014, *AJ*, 148, 42
 Nakamura M., Uchida Y., Hirose S., 2001, *New A*, 6, 61
 Ostorero L., Villata M., Raiteri C. M., 2004, *A&A*, 419, 913
 Otero-Santos J. et al., 2020, *MNRAS*, 492, 5524
 Perucho M., Kovalev Y. Y., Lobanov A. P., Hardee P. E., Agudo I., 2012, *ApJ*, 749, 55
 Peterson B. M., Wanders I., Horne K., Collier S., Alexander T., Kaspi S., Maoz D., 1998, *PASP*, 110, 660
 Raiteri C. M. et al., 1999, *A&A*, 352, 19
 Raiteri C. M. et al., 2001, *A&A*, 377, 396
 Raiteri C. M. et al., 2003, *A&A*, 402, 151
 Raiteri C. M. et al., 2009, *A&A*, 507, 769
 Raiteri C. M. et al., 2013, *MNRAS*, 436, 1530
 Raiteri C. M. et al., 2015, *MNRAS*, 454, 353
 Raiteri C. M. et al., 2017a, *MNRAS*, 466, 3762
 Raiteri C. M. et al., 2017b, *Nature*, 552, 374
 Raiteri C. M. et al., 2021, *MNRAS*, 501, 1100
 Ricker G. R. et al., 2015, *J. Astron. Telesc. Instrum. Syst.*, 1, 014003
 Rieger F. M., 2004, *ApJ*, 615, L5
 Sandrinelli A. et al., 2017, *A&A*, 600, A132
 Scargle J. D., 1982, *ApJ*, 263, 835
 Sillanpaa A., Haarala S., Valtonen M. J., Sundelius B., Byrd G. G., 1988, *ApJ*, 325, 628
 Sillanpaa A. et al., 1996, *A&A*, 315, L13
 Simonetti J. H., Cordes J. M., Heeschen D. S., 1985, *ApJ*, 296, 46
 Smith P. S., 1996, in Miller H. R., Webb J. R., Noble J. C., eds, ASP Conf. Ser. Vol. 110, Blazar Continuum Variability. Astron. Soc. Pac., San Francisco, p. 135
 Sobacchi E., Sormani M. C., Stamerra A., 2017, *MNRAS*, 465, 161
 Stickel M., Fried J. W., Kuehr H., 1993, *A&AS*, 98, 393
 Teräsanta H. et al., 1998, *A&AS*, 132, 305
 Thum C., Agudo I., Molina S. N., Casadio C., Gómez J. L., Morris D., Ramakrishnan V., Sievers A., 2018, *MNRAS*, 473, 2506
 Urry C. M., Padovani P., 1995, *PASP*, 107, 803
 Valtonen M., Pihajoki P., 2013, *A&A*, 557, A28
 Vaughan S., 2005, *A&A*, 431, 391
 Vaughan S., Edelson R., Warwick R. S., Uttley P., 2003, *MNRAS*, 345, 1271
 Villata M., Ferrari A., 1994a, *Phys. Plasmas*, 1, 2200
 Villata M., Ferrari A., 1994b, *A&A*, 284, 663
 Villata M., Ferrari A., 1995, *A&A*, 293, 626
 Villata M., Raiteri C. M., 1999, *A&A*, 347, 30
 Villata M., Tsinganos K., 1993, *Phys. Fluids B*, 5, 2153
 Villata M., Tsinganos K., 1994, *Phys. Plasmas*, 1, 216
 Villata M., Raiteri C. M., Sillanpaa A., Takalo L. O., 1998, *MNRAS*, 293, L13
 Villata M. et al., 2002, *A&A*, 390, 407
 Villata M. et al., 2004, *A&A*, 421, 103
 Villata M. et al., 2006, *A&A*, 453, 817
 Villata M. et al., 2008, *A&A*, 481, L79
 Wagner S., Sanchez-Pons F., Quirrenbach A., Witzel A., 1990, *A&A*, 235, L1
 Wagner S. J. et al., 1993, *A&A*, 271, 344
 Weaver Z. R. et al., 2020, *ApJ*, 900, 137
 Wu J., Peng B., Zhou X., Ma J., Jiang Z., Chen J., 2005, *AJ*, 129, 1818
 Zhang H., Li X., Giannios D., Guo F., Liu Y.-H., Dong L., 2020, *ApJ*, 901, 149

APPENDIX A: STRUCTURE FUNCTION ANALYSIS

The SF is here used to validate the results obtained by the ACF in Section 7.1. Figs A1–A3 show the SFs obtained for the detrended light curves shown in Figs 11–13, respectively. As in the ACF case, we also calculated the mean SF and used its maximum and second minimum to set thresholds to identify the most significant SF maxima and minima in the single SFs. These minima/maxima thresholds are 0.945/1.260 for Sector 14, 0.935/1.191 for Sector 20, and 0.961/1.217 for Sector 21. The comparison of the SF minima with the ACF maxima and of the SF maxima with the ACF minima reveal a good agreement, because all ACF time-scales are confirmed by the SFs. Moreover, the SFs reveal some additional signals: some of them were already present in the ACFs, but did not fulfil the requirement to be present in more than three detrended light curves.

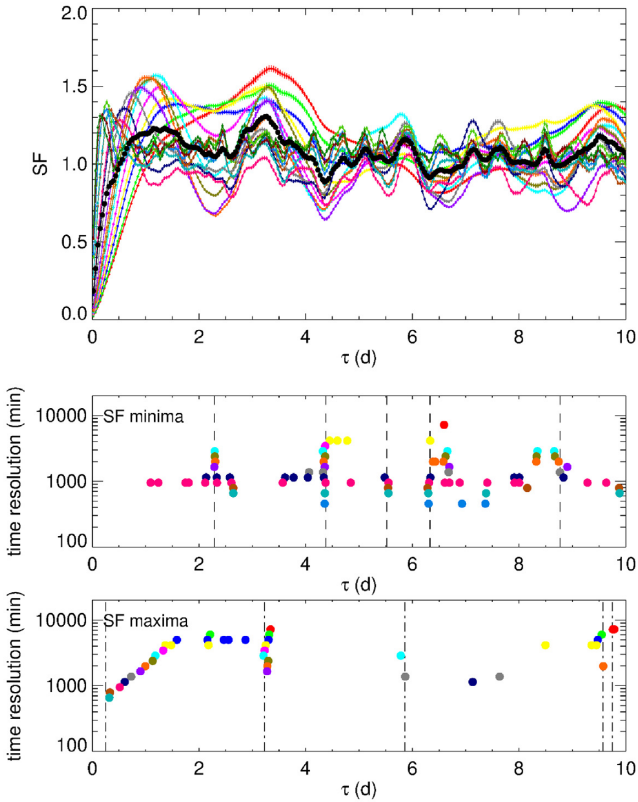


Figure A1. Top panel: the SFs (normalized to their mean value) of the detrended light curves of Sector 14 shown in Fig. 11. The black dots represent the average SF, whose maximum and second minimum are used as thresholds for the significance of the maxima/minima of the single SFs. Middle/Bottom panel: the time lag of the most significant SF minima/maxima versus the time resolution of the spline used to perform the detrending. The vertical lines mark the results obtained with the ACFs in Section 7.1.

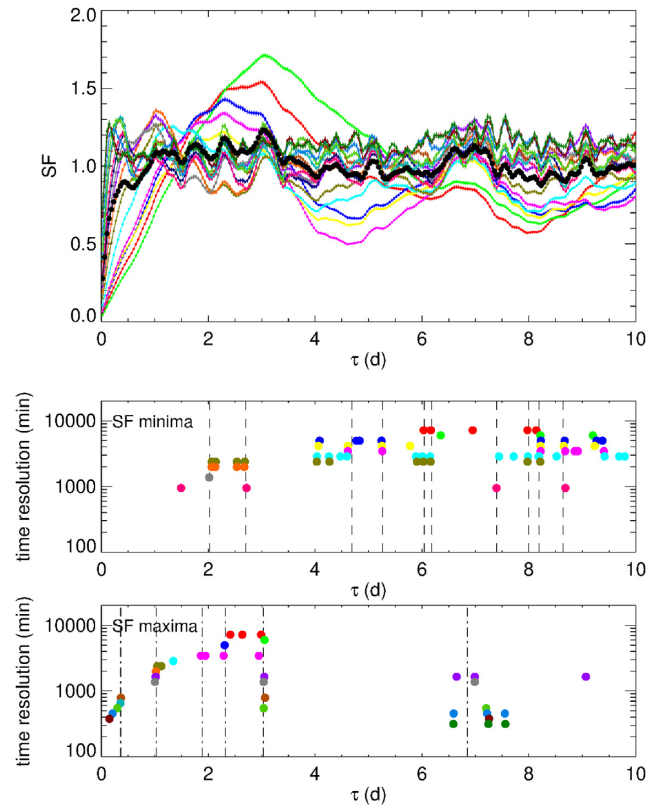


Figure A3. As in Fig. 14, but for Sector 21.

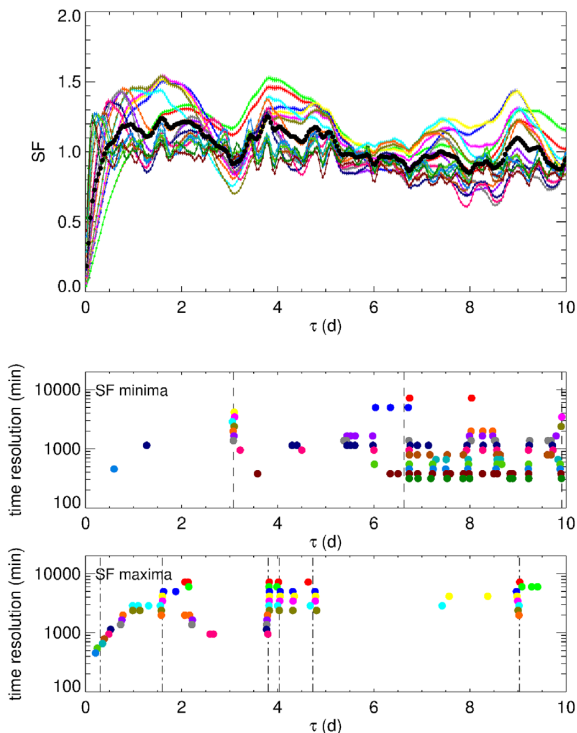


Figure A2. As in Fig. 14, but for Sector 20.

¹INAF, Osservatorio Astrofisico di Torino, via Osservatorio 20, I-10025 Pino Torinese, Italy

²Astronomical Institute, St Petersburg State University, Universitetskij Pr. 28, Petrodvorets, St Petersburg 198504, Russia

³Pulkovo Observatory, St Petersburg 196140, Russia

⁴Institute for Astrophysical Research, Boston University, 725 Commonwealth Avenue, Boston, MA 02215, USA

⁵Instituto de Astrofísica de Canarias, E-38200 La Laguna, Tenerife, Spain

⁶Departamento de Astrofísica, Universidad de La Laguna, E38206 La Laguna, Tenerife, Spain

⁷Instituto de Astrofísica de Andalucía-CSIC, Glorieta de la Astronomía s/n, E-18008 Granada, Spain

⁸Institute of Applied Astronomy RAS, Nab Kutuzova 10, St Petersburg 191187, Russia

⁹Institute of Astronomy and National Astronomical Observatory, Bulgarian Academy of Sciences, 72 Tsarigradsko Shose Blvd., BG-1784 Sofia, Bulgaria

¹⁰Instituto de Astronomía, Universidad Nacional Autónoma de México, AP 70-264, CDMX 04510, Mexico

¹¹Finnish Centre for Astronomy with ESO (FINCA), University of Turku, Quantum, Vesilinnantie 5, FI-20014 University of Turku, Finland

¹²Aalto University Metsähovi Radio Observatory, Metsähovintie 114, FI-02540 Kylmäla, Finland

¹³Department of Electronics and Nanoengineering, Aalto University, P.O. BOX 15500, FI-00076 Aalto, Finland

¹⁴Crimean Astrophysical Observatory RAS, P/O Nauchny 298409, Crimea

¹⁵Faculty of Physics, Department of Astronomy, University of Sofia, BG-1164 Sofia, Bulgaria

¹⁶EPT Observatories, Tifarfe, E-38780 La Palma, Spain

¹⁷INAF, TNG Fundación Galileo Galilei, E-38712 La Palma, Spain

¹⁸Foundation for Research and Technology - Hellas, IESL & Institute of Astrophysics, Voutes, 7110 Heraklion, Greece

¹⁹Department of Physics, University of Crete, 71003 Heraklion, Greece

²⁰*Max Planck Institute for Radio Astronomy, Auf dem Hügel, 69 D-53121 Bonn, Germany*

²¹*Graduate Institute of Astronomy, National Central University, Zhongli 32051, Taoyuan, Taiwan*

²²*Astronomical Observatory, Volgina 7, 11060 Belgrade, Serbia*

²³*INAF, Istituto di Radioastronomia, Via Gobetti 101, I-40129 Bologna, Italy*

²⁴*Aryabhata Research Institute of Observational Sciences (ARIES), Manora Peak, Nainital 263001, India*

²⁵*Instituto de Astronomía, Universidad Nacional Autónoma de México, AP 106, Ensenada 22860, BC, Mexico*

²⁶*Korea Astronomy and Space Science Institute, 776 Daedeok-daero, Yuseong-gu, Daejeon 34055, Republic of Korea*

²⁷*Abastumani Observatory, Mt. Kanobili, 0301 Abastumani, Georgia*

²⁸*Nordic Optical Telescope, Apartado 474, E-38700 Santa Cruz de La Palma, Spain*

²⁹*Observatoire de Genève, Université de Genève, Chemin Pegasi 51, CH-1290 Versoix, Switzerland*

³⁰*Landessternwarte, Zentrum für Astronomie der Universität Heidelberg, Königstuhl 12, D-69117 Heidelberg, Germany*

³¹*Engelhardt Astronomical Observatory, Kazan Federal University, Tatarstan, Russia*

³²*Samtskhe-Javakheti State University, 92 Shota Rustaveli St Akhaltsikhe, Georgia*

³³*Faculty of Mathematics, University of Belgrade, Studentski trg 16, 11000 Belgrade, Serbia*

³⁴*Instituto de Radioastronomía Milimétrica, Avenida Divina Pastora, 7, Núcleo Central, E-18012 Granada, Spain*

³⁵*Department of Physics and Mathematics, Aoyama Gakuin University, 5-10-1 Fuchinobe, Chuo-ku, Sagami-hara, Kanagawa 252-5258, Japan*

³⁶*Special Astrophysical Observatory, Russian Academy of Sciences, Nizhny Arkhyz 369167, Russia*

This paper has been typeset from a $\text{\TeX}/\text{\LaTeX}$ file prepared by the author.